LEARNING 3D REPRESENTATIONS OF MOLECULAR CHIRALITY WITH INVARIANCE TO BOND ROTATIONS

Keir Adams, Lagnajit Pattanaik, & Connor W. Coley
Department of Chemical Engineering
Massachusetts Institute of Technology
Cambridge, MA 02139, USA
{keir,lagnajit,ccoley}@mit.edu

ABSTRACT

Molecular chirality, a form of stereochemistry most often describing relative spatial arrangements of bonded neighbors around tetrahedral carbon centers, influences the set of 3D conformers accessible to the molecule without changing its 2D graph connectivity. Chirality can strongly alter (bio)chemical interactions, particularly protein-drug binding. Most 2D graph neural networks (GNNs) designed for molecular property prediction at best use atomic labels to naïvely treat chirality, while E(3)-invariant 3D GNNs are invariant to chirality altogether. To enable representation learning on molecules with defined stereochemistry, we design an SE(3)-invariant model that processes torsion angles of a 3D molecular conformer. We explicitly model conformational flexibility by integrating a novel type of invariance to rotations about internal molecular bonds into the architecture, mitigating the need for multi-conformer data augmentation. We test our model on four benchmarks: contrastive learning to distinguish conformers of different stereoisomers in a learned latent space, classification of chiral centers as R/S, prediction of how enantiomers rotate circularly polarized light, and ranking enantiomers by their docking scores in an enantiosensitive protein pocket. We compare our model, Chiral InterRoto-Invariant Neural Network (ChIRo), with 2D and 3D GNNs to demonstrate that our model achieves state of the art performance when learning chiral-sensitive functions from molecular structures.

1 INTRODUCTION

Advances in graph neural networks (GNNs) have revolutionized molecular representation learning for (bio)chemical applications such as high-fidelity property prediction (Huang et al., 2021; Chuang et al., 2020), accelerated conformer generation (Ganea et al., 2021; Mansimov et al., 2019; Simm & Hernandez-Lobato, 2020; Xu et al., 2021; Pattanaik et al., 2020b), and molecular optimization (Elton et al., 2019; Brown et al., 2019). Fueling recent developments have been efforts to model shape-dependent physio-chemical properties by learning directly from molecular conformers (snapshots of 3D molecular structures) or from 4D conformer ensembles, which better capture molecular flexibility. For instance, recent state-of-the-art GNNs feature message updates informed by bond distances, bond angles, and torsion angles of the input conformer (Schütt et al., 2017; Klicpera et al., 2020b; Liu et al., 2021; Klicpera et al., 2021). However, few studies have considered the expressivity of GNNs when tasked with learning the nuanced effects of molecular stereochemistry, which describes how the relative arrangement of atoms in space differ for molecules with equivalent graph connectivity.

Tetrahedral (point) chirality is among the most prevalent types of stereochemistry, and describes the spatial arrangement of chemical substituents around the vertices of a tetrahedron centered on a chiral center, typically a carbon atom with four non-equivalent bonded neighbors. Two molecules which differ only in the relative atomic arrangements around their chiral centers are called stereoisomers, or enantiomers if they can be interconverted through reflection across a plane. Enantiomers are distinguished in chemical line drawings by a dashed or bold wedge indicating whether a bonded neighbor to a chiral center is directed into or out of the page (Figure 1A). Although enantiomers share many chemical properties such as boiling/melting points, electronic energies, and solubility in
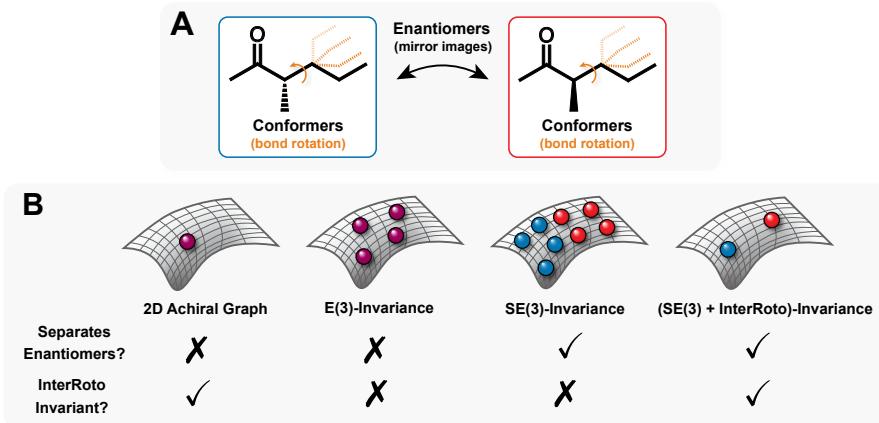
Figure 1: Schematic of how different conformers of two enantiomers (panel A) separate in a learned latent space (panel B) under a 2D (achiral) graph model, E(3)- and SE(3)-invariant 3D models, and ChIRo, which integrates invariance to rotations about internal bonds.

most solvents, enantiomers can display strikingly different behavior when interacting with external chiral environments. For instance, chirality is critical for pharmaceutical drug design (Nguyen et al., 2006; Jamali et al., 1989), where protein-ligand interactions may be highly influenced by ligand chirality, as well for designing structure-directing agents for zeolite growth (Luis & Beatriz, 2018) and for optimizing enantioselective catalysts (Pfaltz & Drury, 2004; Liao et al., 2018).

Chiral centers are inverted upon reflection through a mirror plane. Consequently, E(3)-invariant 3D GNNs that only consider pairwise atomic distances or bond angles in their message updates, such as SchNet (Schütt et al., 2017) and DimeNet/DimeNet++ (Klicpera et al., 2020a;b), are inherently limited in their ability to distinguish enantiomers (Figure 1B). Although SE(3)-invariant 3D GNNs, such as the recently proposed SphereNet (Liu et al., 2021) and GemNet (Klicpera et al., 2021), can in theory learn chirality, their expressivity in this setting has not been explored.

Alongside the development of 3D GNNs, which process individual 3D conformers, there have been efforts to better represent conformational flexibility by encoding multiple conformers in a 4D (multi-instance) ensemble for property prediction (Zankov et al., 2021; 2019; Axelrod & Gomez-Bombarelli, 2021), identifying important conformer poses (Chuang & Keiser, 2020), and predicting solvation energies (Weinreich et al., 2021). Unless in the solid state, molecules are not rigid objects or static 2D graphs, but are flexible structures that continuously interconvert through rapid rotations of chemical bonds as well as through a number of smaller perturbations such as bond stretching, bending, and wagging. Explicitly modeling this probability distribution over accessible conformer space has the potential to drastically improve the modeling of protein-drug interactions, where the most relevant active pose of the ligand is not known *a priori*, as well as in the prediction of Boltzmann-averages, which depend on a distribution of conformers. One challenge with these methods is selecting which conformers to include in an ensemble: the space of accessible conformations combinatorially explodes with the number of rotatable bonds, and important poses are not known *a priori*. Modeling flexibility with multi-instance methods thus requires explicit conformer enumeration, increasing cost of training/inference without guaranteeing performance gains. Apart from 2D methods, which ignore 3D information altogether, no studies have explicitly modeled conformational flexibility directly within a model architecture.

To explicitly model tetrahedral chirality and conformational flexibility, we design a neural framework to augment 2D GNNs with processing of the SE(3)-invariant internal coordinates of a conformer, namely bond distances, bond angles, and torsion angles. Our specific contributions are:

- We design a method for graph neural networks to learn the relative orientations of substituents around tetrahedral chiral centers directly from 3D torsion angles

- We introduce a novel invariance to internal rotations of rotatable bonds directly into a model architecture, potentially mitigating the need for 4D ensemble methods or conformer-based data augmentation to treat conformational flexibility of molecules

- We propose a contrastive learning framework to probe the ability of SE(3)-invariant 3D graph neural networks to differentiate stereoisomers in a learned latent space
- Through our ablation study, we demonstrate that a global node aggregation scheme, adapted from Winter et al. (2021), which exploits subgraphs based on internal coordinate connectivity can provide a simple way to improve GNNs for chiral property prediction

We explore multiple tasks to benchmark the ability of graph-based neural methods to learn the effects of chirality. Our self-supervised contrastive learning task is the first of its kind applied to clustering multiple 3D conformers of different stereoisomers in a learned latent space. Following Pattanaik et al. (2020a), we also employ a toy R/S chiral label classification task as a necessary but not sufficient test of chiral recognition. For a harder classification task, we follow Mamede et al. (2021) in predicting how enantiomers experimentally rotate circularly polarized light. Lastly, we create a dataset of simulated docking scores to rank small enantiomeric ligands by their binding affinities in an enantiosensitive protein environment. We make our datasets for the contrastive learning, R/S classifaction, and docking tasks available to the public. Comparisons with 2D baselines and the SE(3)-invariant SphereNet demonstrate that our model, **Ch**iral **I**nter**Ro**to-Invariant Neural Network (ChIRo), achieves state-of-the-art performance in 3D chiral molecular representation learning.

2 RELATED WORK

Message passing neural networks. Gilmer et al. (2017) introduced a framework for using GNNs to embed molecules into a continuous latent space for property prediction. In the typical 2D message passing scheme, a molecule is modeled as a discrete 2D graph G with atoms as nodes and bonds as edges. Nodes and edges are initialized with features $\mathbf{x}_i$ and $\mathbf{e}_{ij}$ to embed initial node states:

$$\mathbf{h}_i^0 = U_0(\mathbf{x}_i, \{\mathbf{e}_{ij}\}_{j \in N(i)}) \tag{1}$$

where $N(i)$ denotes the neighboring atoms of node i. In each layer t of message passing, node states are updated with aggregated messages from neighboring nodes. After T layers, graph feature vectors are constructed from some (potentially learnable) aggregation over the learned node states. A readout phase then uses this graph embedding for downstream property prediction:

$$\mathbf{h}_i^{t+1} = U_t(\mathbf{h}_i^t, \mathbf{m}_i^{t+1}), \quad \mathbf{m}_i^{t+1} = \sum_{j \in N(i)} M_t(\mathbf{h}_i^t, \mathbf{h}_j^t, \mathbf{e}_{ij}) \tag{2}$$

$$\hat{y} = \text{Readout}(\mathbf{g}), \quad \mathbf{g} = Agg(\{\mathbf{h}_i^T | i \in G\}) \tag{3}$$

There exist many variations on this basic message passing framework (Duvenaud et al., 2015; Kearnes et al., 2016). In particular, Yang et al. (2019)'s directed message passing neural network (DMPNN, or ChemProp) based on Dai et al. (2016) learns edge-based messages $\mathbf{m}_{ij}^t$ and updates edge embeddings $\mathbf{h}_{ij}^t$ rather than node embeddings. The Graph Attention Network (Veličković et al., 2018) constructs message updates $\mathbf{m}_i^t$ using attention pooling over local node states.

3D Message Passing and Euclidean Invariances. 3D GNNs differ in their message passing schemes by using molecular internal coordinates (distances, angles, torsions) to pass geometry-informed messages between nodes. It is important to use 3D information that is at least SE(3)-invariant, as molecular properties are invariant to global rotations or translations of the conformer.

SchNet (Schütt et al., 2017), a well-established network for learning quantum mechanical properties of 3D conformers, updates node states using messages informed by radial basis function expansions of interatomic distances between neighboring nodes. DimeNet (Klicpera et al., 2020b) and its newer variant DimeNet++ (Klicpera et al., 2020a) exploit additional molecular geometry by using spherical Bessel functions to embed angles ϕ_{ijk} between the edges formed between nodes i and j and nodes j and $k \neq i$ in the directed message updates to node i.

SchNet and DimeNet are E(3)-invariant, as pairwise distances and angles formed between two edges are unchanged upon global rotations, translations, and *reflections*. Since enantiomers are mirror images, SchNet and DimeNet are therefore invariant to this form of chirality. To be SE(3)-invariant, 3D GNNs must consider torsion angles, denoted ψ_{ixyj}, between the planes defined by angles ϕ_{ixy} and ϕ_{xyj}, where i, x, y, j are four sequential nodes along a simple path. Torsion angles are negated upon reflection, and thus models considering all torsion angles should be implicitly sensitive to

chirality. Flam-Shepherd et al. (2020), Liu et al. (2021) (SphereNet), and Klicpera et al. (2021) (GemNet) introduce 3D GNNs that all embed torsions in their message updates.

Using a complete set of torsion angles provides access to the full geometric information present in the conformer but does not guarantee expressivity when learning chiral-dependent functions. Torsions are negated upon reflection, but any given torsion can also be changed via simple rotations of a rotatable bond–which changes the conformation, but not the molecular identity (i.e., chirality does not change). Reflecting a non-chiral conformer will also negate its torsions, but the reflected conformer can be reverted to its original structure via rotations about internal bonds. To understand chirality, neural models must learn how *coupled* torsions, the set of torsions $\{\psi_{ixyj}\}_{(i,j)}$ that share a bond between nodes x and y (with x or y being chiral), collectively differ between enantiomers.

E(3)- and SE(3)-Equivariant Neural Networks. Recent work has introduced *equivariant* layers into graph neural network architectures to explicitly model how global rotations, translations, and (in some cases) reflections of a 3D structure transform tensor properties, such as molecular dipoles or force vectors. SE(3)-equivariant models (Fuchs et al., 2020; Thomas et al., 2018) should be sensitive to chirality, while E(3)-equivariant models (Satorras et al., 2021) will only be sensitive if the output layer is *not* E(3)-invariant. Since we use SE(3)-invariant internal coordinates as our 3D representation, we only compare our model to other SE(3)- or E(3)-invariant 3D GNNs.

Explicit representations of chirality in machine learning models. A number of machine learning studies account for chirality through hand-crafted molecular descriptors (Schneider et al., 2018; Golbraikh et al., 2001; Kovatcheva et al., 2007; Valdés-Martiní et al., 2017; Mamede et al., 2021). A naïve but common method for making 2D GNNs sensitive to chirality is through the inclusion of chiral tags as node features. *Local* chiral tags describe the orientation of substituents around chiral centers (CW or CCW) given an ordered list of neighbors. *Global* chiral tags use the Cahn-Ingold-Prelog (CIP) rules for labeling the handedness of chiral centers as R ("rectus") or S ("sinister"). It is unclear whether (and how) models can suitably learn chiral-dependent functions when exposed to these tags as the only indication of chirality. Pattanaik et al. (2020a) propose changing the symmetric message aggregation function in 2D GNNs (sum/max/mean) to an asymmetric function tailored to tetrahedral chiral centers, but this method does not learn chirality from 3D molecular geometries.

Chirality in 2D Vision and 3D Pose Estimation. Outside of molecular chirality, there has been work in the deep learning community to develop neural methods that learn chiral representations for 2D image recognition (Lin et al., 2020) and 3D human pose estimation (Yeh et al., 2019). In particular, Yeh et al. (2019) consider integrating equivariance to chiral transforms directly into neural architectures including feed forward layers, LSTMs/GRUs, and convolutional layers.

3 CHIRAL INTERROTO-INVARIANT NEURAL NETWORK (CHIRO)

Our model comprises a 2D message passing phase to embed node states based on graph connectivity, two feed-forward networks based on Winter et al. (2021) to encode 3D bond distances and bond angles, a specially designed torsion encoder inspired by Ganea et al. (2021) to explicitly encode chirality with invariance to internal bond rotations (InterRoto-invariance), and a readout phase for property prediction. Figure 2 visualizes how we encode torsion angles to achieve an InterRoto invariant representation of chirality, which constitutes the core of ChIRo. The full model is visualized in appendix A.4. We implement our network with Pytorch Geometric (Fey & Lenssen, 2019). Our source code is available at `https://github.com/keiradams/ChIRo`.

2D Graph Encoder. Given a molecular conformer, we initialize a 2D graph G where nodes are atoms initialized with features $\mathbf{x}_i$ and edges are bonds initialized with features $\mathbf{e}_{ij}$. We treat all hydrogens implicitly, use undirected edges, and omit chiral atom tags and bond stereochemistry tags. $\mathbf{x}_i$ include the atomic mass and one-hot encodings of atom type, formal charge, degree, number of hydrogens, and hybridization state. $\mathbf{e}_{ij}$ include one-hot encodings of the bond type, whether the bond is conjugated, and whether the bond is in a ring system. In select experiments, we include global and local chiral atom tags and bond stereochemistry tags for performance comparisons.

As in Winter et al. (2021), we use Simonovsky & Komodakis (2017)'s edge-conditioned convolution (EConv) to embed the initial node features with the edge features:

$$\mathbf{h}_i^0 = \mathbf{\Theta}\mathbf{x}_i + \sum_{j \in N(i)} \mathbf{x}_j \cdot f_e(\mathbf{e}_{ij}) \tag{4}$$
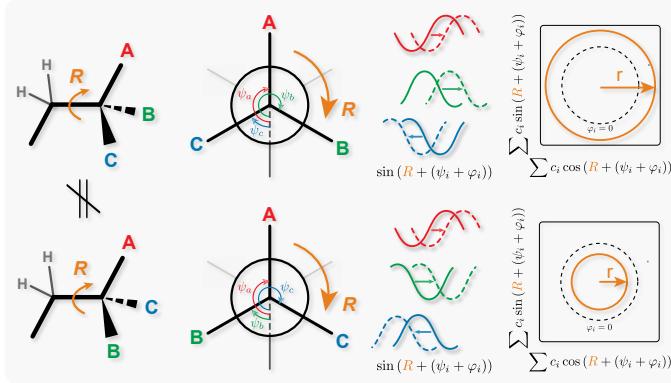
Figure 2: Demonstration of how ChIRo learns chiral representations. Given two enantiomers with three coupled torsions ψ_a, ψ_b, and ψ_c involving a chiral center, rotating the shared carbon-carbon bond by $R \in [0, 2\pi)$ rotates each torsion together, forming three periodic sinusoids. Learning phase shifts φ_i for each torsion produces shifted waves that differ between enantiomers. A weighted sum of the shifted sinusoids results in different degrees of wave interference between enantiomers, yielding different amplitudes of the net waves. These amplitudes, visualized here by the different radii of the circles formed by plotting the summed sines against the summed cosines, are invariant to the rotation of the internal carbon-carbon bond. See appendices A.1, A.2 for further details.

where $\boldsymbol{\Theta}$ is a learnable weight matrix and f_e is a multi-layer perceptron (MLP). Node states $\mathbf{h}_i^t \in \mathbb{R}^{h_t}$ are then updated through T sequential Graph Attention Layers (GAT) (Veličković et al., 2018):

$$\mathbf{h}_i^t = \text{GAT}^{(t)}(\mathbf{h}_i^{t-1}, \{\mathbf{h}_j^{t-1}\}_{j \in N(i)}), \quad t = 1, ..., T \tag{5}$$

Bond Distance and Bond Angle Encoders. To embed 3D bond distance and bond angle information, we follow Winter et al. (2021) by individually encoding each bond distance d_{ij} (in Angstroms) and angle ϕ_{ijk} into learned latent vectors. We then sum-pool these vectors to get conformer-level latent embeddings $\mathbf{z}_d \in \mathbb{R}^z$ and $\mathbf{z}_\phi \in \mathbb{R}^z$:

$$\mathbf{z}_d = \sum_{(i,j) \in G} f_d(\mathbf{h}_i, \mathbf{h}_j, d_{ij}) + f_d(\mathbf{h}_j, \mathbf{h}_i, d_{ij}) \tag{6}$$

$$\mathbf{z}_\phi = \sum_{(i,j,k) \in G} f_\phi(\mathbf{h}_i, \mathbf{h}_j, \mathbf{h}_k, \cos \phi_{ijk}, \sin \phi_{ijk}) + f_\phi(\mathbf{h}_k, \mathbf{h}_j, \mathbf{h}_i, \cos \phi_{ijk}, \sin \phi_{ijk}) \tag{7}$$

where f_d and f_ϕ are MLPs and $(., .)$ denotes concatenation. We maintain invariance to node ordering by encoding both (i, j) and (j, i) for each distance d_{ij}, and both (i, j, k) and (k, j, i) for each angle ϕ_{ijk}. For experiments that mask all internal coordinates (i.e., set all bond lengths and angles to 0), $\mathbf{z}_d$ and $\mathbf{z}_\phi$ represent aggregations of 2D node states based on subgraphs of local atomic connectivity.

Torsion Encoder. We specially encode torsion angles to achieve two desired properties: 1) an invariance to rotations about internal molecular bonds, and 2) the ability to learn molecular chirality. Both of these properties depend critically on how the model treats *coupled* torsion angles–torsions that cannot be independently rotated in the molecular conformer. For instance, torsions ψ_a, ψ_b, and ψ_c in Figure 2 are coupled, as rotating the internal carbon-carbon bond rotates each torsion simultaneously. Symmetrically aggregating *every* torsion does not respect this inherent coupling. However, only encoding a subset of non-redundant torsions–a minimal set that completely define the structure of the conformer–would make the model sensitive to which arbitrary subset was selected.

Ganea et al. (2021) provide a partial solution to this problem in their molecular conformer generator, which we adapt below. Rather than encoding each torsion individually, they compute a weighted sum of the cosines and sines of each coupled torsion, where the weights are predicted by a neural network[1]. Formally, given an internal (non-terminal) molecular bond between nodes x and y that

---

[1]Ganea et al. (2021) use an *untrained* network with randomized parameters to predict the weighting coefficients. Instead, we learn the parameters in f_c and compare these approaches in Appendix A.8.

yields a set of coupled torsions $\{\psi_{ixyj}\}_{(i,j)}$ for $i \in N(x) \setminus \{y\}$ and $j \in N(y) \setminus \{x\}$, they compute:

$$(\alpha_{\cos}^{(xy)}, \alpha_{\sin}^{(xy)}) = \sum_{i \in N(x) \setminus \{y\}} \sum_{j \in N(y) \setminus \{x\}} c_{ij}^{(xy)} \cdot \bigg(\cos(\psi_{ixyj}), \sin(\psi_{ixyj}) \bigg) \qquad (8)$$

$$c_{ij}^{(xy)} = \sigma \bigg(f_c(\mathbf{h}_i, \mathbf{h}_x, \mathbf{h}_y, \mathbf{h}_j) + f_c(\mathbf{h}_j, \mathbf{h}_y, \mathbf{h}_x, \mathbf{h}_i) \bigg) \qquad (9)$$

where f_c is an MLP that maps to $\mathbb{R}$. Note that the sigmoid activation σ, which keeps each $c_{ij}^{(xy)}$ bounded to $(0, 1)$, is our addition.

Because rotating the bond (x, y) rotates the torsions $\{\psi_{ixyj}\}$ together, the sinusoids $\{\sin(\psi_{ixyj})\}_{(i,j)}$ and $\{\cos(\psi_{ixyj})\}_{(i,j)}$ have the same frequency. Therefore, the weighted sums of these cosines and sines are also sinusoids, which when plotted against each other as a function of rotating bond (x, y), form a perfect circle (appendix A.1). Critically, the radius of this circle, $||\alpha_{\cos}^{(xy)}, \alpha_{\sin}^{(xy)}||$, is invariant to the action of rotating bond (x, y) (Figure 2). We therefore encode these radii in order to achieve invariance to how any bond in the conformer is rotated.

The above formulation, as presented, is also invariant to chirality (appendix A.2). To break this symmetry, we add a learned phase shift, φ_{ixyj}, to each torsion ψ_{ixyj}:

$$(\cos \varphi_{ixyj}, \sin \varphi_{ixyj}) = \ell_2{}^{\text{norm}} \bigg(f_\varphi(\mathbf{h}_i, \mathbf{h}_x, \mathbf{h}_y, \mathbf{h}_j) + f_\varphi(\mathbf{h}_j, \mathbf{h}_y, \mathbf{h}_x, \mathbf{h}_i) \bigg) \qquad (10)$$

$$(\alpha_{\cos}^{(xy)}, \alpha_{\sin}^{(xy)}) = \sum_{i \in N(x) \setminus \{y\}} \sum_{j \in N(y) \setminus \{x\}} c_{ij}^{(xy)} \cdot \bigg(\cos(\psi_{ixyj} + \varphi_{ixyj}), \sin(\psi_{ixyj} + \varphi_{ixyj}) \bigg) \quad (11)$$

where f_φ is an MLP that maps to $\mathbb{R}^2$ and $\ell_2{}^{\text{norm}}$ indicates L2-normalization. Because enantiomers have the same 2D graph, the learned coefficients $c_{ij}^{(xy)}$ and phase shifts φ_{ixyj} are identical between enantiomers (if $\mathbf{x}_i$ is initialized without chiral tags). However, because enantiomers have different spatial orientations of atoms around chiral centers, the relative values of coupled torsions around bonds involving those chiral centers also differ (Figure 2). As a result, learning phase shifts creates different degrees of wave-interference when summing the weighted cosines and sines for inverted chiral centers. The amplitudes of the net waves (corresponding to radius $||\alpha_{\cos}^{(xy)}, \alpha_{\sin}^{(xy)}||$) will differ between enantiomers, allowing our model to encode different radii for different enantiomers.

With this torsion aggregation scheme, we complete our torsion encoder by individually encoding each internal molecular bond, along with its learned radius, into a latent vector and sum-pooling:

$$\mathbf{z}_\alpha = \sum_{(x,y) \in G} \mathbf{z}_{\alpha_{xy}}, \quad \mathbf{z}_{\alpha_{xy}} = f_\alpha \bigg(\mathbf{h}_x, \mathbf{h}_y, \Big\| \alpha_{\cos}^{(xy)}, \alpha_{\sin}^{(xy)} \Big\| \bigg) + f_\alpha \bigg(\mathbf{h}_y, \mathbf{h}_x, \Big\| \alpha_{\cos}^{(xy)}, \alpha_{\sin}^{(xy)} \Big\| \bigg) \quad (12)$$

Readout. For property prediction, we concatenate the sum-pooled node states with the conformer embedding components $\mathbf{z}_d$, $\mathbf{z}_\phi$, and $\mathbf{z}_\alpha$, capturing embeddings of bond lengths, angles, and torsions, respectively. This concatenated representation is then fed through a feed-forward neural network:

$$\hat{y} = f_{\text{out}} \left(\sum_{i \in G} \mathbf{h}_i, \mathbf{z}_d, \mathbf{z}_\phi, \mathbf{z}_\alpha \right) \qquad (13)$$

Appendix A.3 explores the option of propagating the learned 3D representations of chirality to node states prior to sum-pooling via additional message passing, treating each $\mathbf{z}_{\alpha_{xy}}$ as a vector of edge-attributes. This stage of chiral message passing (CMP) is designed to help propagate local chiral representations across the molecular graph, and to provide an alternative method of augmenting 2D GNNs which include chiral tags as atom features. However, CMP does not significantly affect ChIRo's performance across the tasks considered and is thus not included in our default model.

4 EXPERIMENTS

We evaluate the ability of our model to learn chirality with four distinct tasks: contrastive learning to distinguish between 3D conformers of different stereoisomers in a learned latent space, classifying
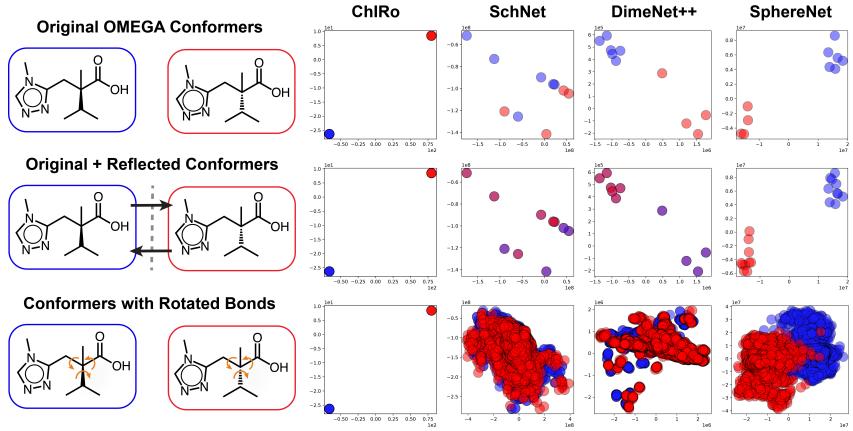
Figure 3: Visualization of how conformers of two enantiomers in the contrastive learning test set cluster in the learned latent space for ChIRo, SchNet, DimeNet++, and SphereNet (top row) using the original OMEGA-generated conformers, (middle row) upon reflecting the conformers, and (bottom row) upon rotating internal bonds involving the chiral center. Unlike SchNet, DimeNet++, and even the SE(3)-invariant SphereNet, ChIRo maintains perfect separation between stereoisomers across these conformer transformations.

enantiomer chiral centers as R/S, predicting how enantiomers rotate circularly polarized light, and ranking enantiomers by their docking scores in a chiral protein environment. We compare our model with 2D baselines including DMPNN with chiral atom tags (Yang et al., 2019), and Tetra-DMPNN with and without chiral atom tags (Pattanaik et al., 2020a). We also compare our model to 3D GNN baselines, including the E(3)-invariant SchNet and DimeNet++, and the SE(3)-invariant SphereNet.

Contrastive Learning to Distinguish Stereoisomers. For contrastive learning, we use a subset of the PubChem3D dataset, which consists of multiple OMEGA-generated conformations of organic molecules with up to 50 heavy atoms and 15 rotatable bonds (Bolton et al., 2011; Hawkins et al., 2010). Our subset consists of 2.98M conformers of 598K stereoisomers of 257K 2D graphs. Each stereoisomer has at least two conformers, and each graph has at least two stereoisomers. We create 70/15/15 training/validation/test splits, keeping conformers corresponding to the same 2D graphs in the same data partition. See appendix A.5 for full training details.

We formulate this task to answer the following question: can the model learn to cluster conformers sharing the same (chiral) molecular identity in a learned latent space, while distinguishing clusters belonging to different stereoisomers of a shared 2D graph? We train each model with a triplet margin loss (Balntas et al., 2016) with a normalized Euclidean distance metric:

$$\mathcal{L}_{\text{triplet}} = \max(0, d(\mathbf{z}_a, \mathbf{z}_p) - d(\mathbf{z}_a, \mathbf{z}_n) + 1), \ \ d(\mathbf{z}_1, \mathbf{z}_2) = \left\| \frac{\mathbf{z}_1}{\|\mathbf{z}_1\|} - \frac{\mathbf{z}_2}{\|\mathbf{z}_2\|} \right\| \qquad (14)$$

where $\mathbf{z}_a$, $\mathbf{z}_p$, $\mathbf{z}_n$ are learned latent vectors of anchor, positive, and negative examples. For each triplet, we randomly sample a conformer a of stereoisomer i as the anchor, a conformer $p \neq a$ of stereoisomer i as the positive, and a conformer n of stereoisomer $j \neq i$ as the negative, where i and j share the same 2D graph. For ChIRo, we use $\mathbf{z} = \mathbf{z}_\alpha$. For SchNet, DimeNet++, and SphereNet, we use aggregations of node states (out_channels) as $\mathbf{z}$. We set $\mathbf{z} \in \mathbb{R}^2$ to visualize the latent space.

Figure 3 visualizes how conformers of two enantiomers in the test set separate in the latent space for ChIRo, SchNet, DimeNet++, and SphereNet. We explore how this separation is affected upon reflecting the conformers (which inverts chirality) and rotating bonds around the chiral center. By design, ChIRo maintains perfect separation across these transforms. While SchNet and DimeNet++ may seem to superficially separate the original conformers, the separation collapses upon reflection and rotation due to their E(3)-invariance. SphereNet learns good separation that persists through reflection, but the clusters overlap upon rotation of internal bonds. This emphasizes that 3D GNNs have limited chiral expressivity when not explicitly considering *coupled* torsions in message updates.

Classifying Tetrahedral Chiral Centers as R/S. As a simple test of chiral perception for SchNet, DimeNet++, SphereNet and ChIRo, we test whether these 3D models can classify tetrahedral chiral

centers as R/S. We use a subset of PubChem3D containing 466K conformers of 78K enantiomers with one tetrahedral chiral center. We create 70/15/15 train/validation/test splits, keeping conformers corresponding to the same 2D graphs in the same partition. We train with a cross-entropy loss and sample one conformer per enantiomer in each batch. See Appendix A.5 for full training details.

Table 1 reports classification accuracies when evaluating on *all* conformers in the test set, without conformer-based averaging. The SE(3)-invariant ChIRo and SphereNet both reach $> 98\%$ accuracy, whereas the E(3)-invariant SchNet and DimeNet++ fail to learn this simple representation of chirality. We emphasize that we view this classification task as necessary but not sufficient to demonstrate that a model can learn a meaningful representation of chiral molecules.

Table 1: R / S classification accuracy on the test set for ChIRo and 3D GNN baselines. Mean and standard deviations are reported across three trials.

Model	R / S Accuracy (%) ↑
ChIRo	98.5 ± 0.2
SchNet	54.5 ± 0.2
DimeNet++	65.7 ± 2.9
SphereNet	98.2 ± 0.2

Predicting Enantiomers' Signs of Optical Rotation. Enantiomers rotate circularly polarized light in different directions, and the sign of rotation designates the enantiomer as l (levorotatory, $-$) or d (dextrorotatory, $+$). Optical activity is an experimental property, and has no correlation with R/S classifications (Table 15, appendix A.7.2). Following Mamede et al. (2021), who used hand-crafted descriptors to predict l / d labels, we extract 30K enantiomers (15K pairs) with their optical activity in a chloroform solvent from the commercial Reaxys database (Reaxys, Accessed Aug. 6-9, 2021), and generate 5 conformers per enantiomer using the ETKDG algorithm in RDKit (Landrum, 2010). Appendix A.7 describes the filtering procedure. We evaluate with 5-fold cross validation, where each pair of enantiomers are randomly assigned to one of the five folds for testing. In each fold, we randomly split the remaining dataset into 87.5/12.5 training/validation splits, assigning enantiomers to the same data partition. We train with a cross-entropy loss. To characterize how conformer data augmentation affects the performance of ChIRo and SphereNet, we employ two training schemes: the first randomly samples a conformer per enantiomer in each batch; the second uses one pre-sampled conformer per enantiomer. In both schemes, we evaluate on all conformers in the test splits. Appendix A.5 specifies full training details.

Table 2 reports the classification accuracies for each model. Notably, ChIRo outperforms SphereNet by a significant 14%. Also, whereas ChIRo's performance does not suffer when only one conformer per enantiomer is used, SphereNet's performance drops by 10%. This may be due to SphereNet confusing differences in conformational structure versus chiral identities when evaluating pairs of enantiomers. The consistent performance of ChIRo emphasizes its inherent modeling of conformational flexibility without need for data augmentation. Additionally, ChIRo offers significant improvement over DMPNN, demonstrating that our torsion encoder yields a more expressive representation of chirality than simply including chiral tags in node features. The (smaller) improvements over Tetra-

Table 2: Comparisons of ChIRo with baselines when classifying enantiomers as l / d and ranking enantiomers by their docking scores. Mean accuracies and standard deviations are reported on the test sets across 5 folds (l / d) or three trials (enantiomer ranking).

Model	Accuracy (%) ↑	
	l / d	Enantiomer Ranking
ChIRo	$\mathbf{79.3 \pm 0.4}$	$\mathbf{72.0 \pm 0.5}$
ChIRo (1-Conformer)	79.1 ± 0.5	71.9 ± 0.3
SphereNet	65.5 ± 2.4	68.6 ± 0.3
SphereNet (1-Conformer)	55.2 ± 0.3	63.0 ± 0.1
DMPNN with Chiral Tags	74.4 ± 0.8	65.9 ± 0.6
Tetra-DMPNN (permute)	70.2 ± 0.7	66.1 ± 0.3
Tetra-DMPNN (concatenate)	72.6 ± 0.7	68.5 ± 0.3
Tetra-DMPNN (permute) with Chiral Tags	75.6 ± 1.3	67.6 ± 0.6
Tetra-DMPNN (concatenate) with Chiral Tags	76.5 ± 0.8	70.1 ± 0.5

Table 3: Effects of ablating components of ChIRo on test-set accuracies for the l / d classification and enantiomer docking score ranking tasks. Mean and standard deviations are reported across 5 folds (l / d) or 3 repeated trials (enantiomer ranking). The first row indicates the original ChIRo.

Model Components			Accuracy (%) ↑	
Tags	$(d_{ij}, \phi_{ijk}, \psi_{ixyj})$	$(\mathbf{z}_d, \mathbf{z}_\phi, \mathbf{z}_\alpha)$	l / d	Enantiomer Ranking
X	✓	✓	$\mathbf{79.3 \pm 0.4}$	$\mathbf{72.0 \pm 0.5}$
✓	✓	✓	77.7 ± 0.8	71.3 ± 0.7
✓	X	✓	76.2 ± 0.6	68.4 ± 0.9
✓	X	X	70.0 ± 0.6	63.7 ± 0.2
X	X	✓	50.0 ± 0.0	49.6 ± 0.3

DMPNN, which was specially designed to treat tetrahedral chirality in 2D GNNs, suggest that using 3D information to encode chirality is more powerful than 2D representations of chirality.

Ranking Enantiomers by Binding Affinity in a Chiral Protein Pocket. *In silico* docking simulations are widely used to screen drug-ligand interactions, especially in high-throughput virtual screens. However, docking scores can be highly sensitive to the conformation of the docked ligand, which creates a noisy background from which to extract meaningful differences in docking scores between enantiomers. To partially control for this stochasticity, we source conformers of 200K pairs of small (MW $\leq$ 225, # of rotatable bonds $\leq$ 5) enantiomers with only 1 chiral center from PubChem3D (Bolton et al., 2011). We use AutoDock Vina (Trott & Olson, 2010) to dock each enantiomer in a small docking box (PDB ID: 4JBV) three times, and select pairs for which both enantiomers have a range of docking scores $\leq$ 0.1 kcal/mol across the three trials. Finally, we filter pairs of enantiomers whose difference in (best) scores is $\geq$ 0.3 kcal/mol to form a dataset of enantiosensitive docking scores. Each conformer for an enantiomer is assigned the same (best) score. This treats docking score as a stereoisomer-level property. Our final dataset includes 335K conformers of 69K enantiomers (34.5K pairs), which we split into 70/15/15 training/validation/test splits, keeping enantiomers in the same data partition. We train with a mean squared error loss and either randomly sample a conformer per enantiomer in each batch or use one pre-selected conformer per enantiomer. Appendix A.5 specifies full training details. Note that we evaluate the ranking accuracy of the predicted *conformer-averaged* docking scores between enantiomers in the test set.

ChIRo outperforms SphereNet in ranking enantiomer docking scores, achieving an accuracy of 72% (Table 2). This performance is fairly consistent when evaluating ChIRo on subsets of enantiomers which have various differences in their ground-truth scores (Figure 12, appendix A.9). SphereNet once again suffers a drop in performance without conformer data augmentation, whereas ChIRo's performance remains high without such augmentation. ChIRo also outperforms the 2D baselines, with performance gains similar to those in the l / d classification task.

Ablation Study. To investigate how different components of ChIRo contribute to its performance on the l / d classification and ranking tasks, we ablate various components of our model including whether stereochemical tags are included in the atom/bond intializations, whether internal coordinates are masked-out (set to zero), and whether the conformer latent vectors $\mathbf{z}_d$, $\mathbf{z}_\phi$, and $\mathbf{z}_\alpha$ are used during readout (Table 3). Overall, when internal coordinates are masked, including $(\mathbf{z}_d, \mathbf{z}_\phi, \mathbf{z}_\alpha)$ in readout improves model performance by $\sim$5% on both tasks. This suggests that if chiral tags are used as the only indication of chirality (i.e., 3D information is excluded), using the learned node aggregation scheme provides a simple way to improve the ability of 2D GNNs to learn chiral functions. Notably, adding chiral tags to our unablated model does *not* improve performance, while omitting both chiral tags *and* 3D information yields a 2D achiral graph model without chiral perception.

5 CONCLUSION

In this work we design a method for improving representations of molecular stereochemistry in graph neural networks through encoding 3D bond distances, angles, and torsions. Our torsion encoder learns an expressive representation of tetrahedral chirality by processing coupled torsion angles that share a common bond while simultaneously achieving invariance to rotations about internal

molecular bonds, diminishing the need for conformer-based data augmentation to capture conformational flexibility. Comparisons to the E(3)-invariant SchNet and DimeNet++ and the SE(3)-invariant SphereNet on a variety of tasks (one self-supervised, three supervised) dependent on molecular chirality demonstrate that ChIRo achieves state-of-the-art in learning chiral representations from 3D molecular structures, while also outperforming 2D GNNs. We leave consideration of other types of stereoisomerism, particularly cis/trans isomerism and atropisomerism, to future work.

ETHICS STATEMENT

Advancing representations of molecular chirality and conformational flexibility has the potential to accelerate pharmaceutical drug design, renewable energy development, and progress towards energy-efficient and waste-reducing catalysts, among other areas of scientific research. However, in principle, the same advances could also be used for harmful biological, chemical, or materials research and applications thereof.

REPRODUCIBILITY STATEMENT

Care has been taken to ensure reproducibility of all models and experiments in this paper. In addition to detailing exact model architectures and training details in the appendix, we make source code with exact experimental setups, model implementations, random seeds, and best models for each task available at `https://github.com/keiradams/ChIRo`. For the contrastive learning, R/S classification, and ranking enantiomers by docking score tasks, the exact datasets and splits used in each experiment are available at `https://figshare.com/s/e23be65a884ce7fc8543`. Although copyright restrictions prevent us from releasing the dataset and splits for the l / d classification task, we provide detailed data filtering and processing steps in appendix A.7.

REFERENCES

Takuya Akiba, Shotaro Sano, Toshihiko Yanase, Takeru Ohta, and Masanori Koyama. Optuna: A next-generation hyperparameter optimization framework. In *Proceedings of the 25rd ACM SIGKDD International Conference on Knowledge Discovery and Data Mining*, 2019.

Simon Axelrod and Rafael Gomez-Bombarelli. Molecular machine learning with conformer ensembles. *arXiv preprint arXiv:2012.08452*, 2021.

Vassileios Balntas, Edgar Riba, Daniel Ponsa, and Krystian Mikolajczyk. Learning local feature descriptors with triplets and shallow convolutional neural networks. In Edwin R. Hancock Richard C. Wilson and William A. P. Smith (eds.), *Proceedings of the British Machine Vision Conference (BMVC)*, pp. 119.1–119.11. BMVA Press, September 2016. ISBN 1-901725-59-6. doi: 10.5244/C.30.119. URL `https://dx.doi.org/10.5244/C.30.119`.

Evan E. Bolton, Jie Chen, Sunghwan Kim, Lianyi Han, Siqian He, Wenyao Shi, Vahan Simonyan, Yan Sun, Paul A. Thiessen, Jiyao Wang, Bo Yu, Jian Zhang, and Stephen H. Bryant. PubChem3D: a new resource for scientists. *Journal of Cheminformatics*, 3, 2011.

Nathan Brown, Marco Fiscato, Marwin H.S. Segler, and Alain C. Vaucher. GuacaMol: Benchmarking models for de novo molecular design. *Journal of Chemical Information and Modeling*, 59(3): 1096–1108, 2019.

Kangway V. Chuang and Michael J. Keiser. Attention-based learning on molecular ensembles. *arXiv preprint arXiv:2011.12820*, 2020.

Kangway V. Chuang, Laura M. Gunsalus, and Michael J. Keiser. Learning molecular representations for medicinal chemistry. *Journal of Medicinal Chemistry*, 63:8705–8722, 2020.

Hanjun Dai, Bo Dai, and Le Song. Discriminative embeddings of latent variable models for structured data. *arXiv preprint arXiv:1603.05629*, 2016.

David Duvenaud, Dougal Maclaurin, Jorge Aguilera-Iparraguirre, Rafael Gómez-Bombarelli, Timothy Hirzel, Alán Aspuru-Guzik, and Ryan P. Adams. Convolutional networks on graphs for learning molecular fingerprints. *arXiv preprint arXiv:1509.09292*, 2015.

Daniel C. Elton, Zois Boukouvalas, Mark D. Fuge, and Peter W. Chung. Deep learning for molecular design–a review of the state of the art. *Molecular Systems Design & Engineering*, 4:828–849, 2019.

Matthias Fey and Jan Eric Lenssen. Fast graph representation learning with PyTorch Geometric. *arXiv preprint arXiv:1903.02428*, 2019.

Daniel Flam-Shepherd, Tony Wu, Pascal Friederich, and Alan Aspuru-Guzik. Neural message passing on high order paths. *arXiv preprint arXiv:2002.10413*, 2020.

Fabian Fuchs, Daniel Worrall, Volker Fischer, and Max Welling. SE(3)-transformers: 3D roto-translation equivariant attention networks. *NeurIPS*, 2020.

Octavian-Eugen Ganea, Lagnajit Pattanaik, Connor W. Coley, Regina Barzilay, Klavs F. Jensen, William H. Green, and Tommi S. Jaakola. GeoMol: Torsional geometric generation of molecular 3D conformer ensembles. *arXiv preprint arXiv:2106.07802*, 2021.

Justin Gilmer, Samuel S. Schoenholz, Patrick F. Riley, Oriol Vinyals, and George E. Dahl. Neural message passing for quantum chemistry. *arXiv preprint arXiv:1704.01212*, 2017.

Alexander Golbraikh, Danail Bonchev, and Alexander Tropsha. Novel chirality descriptors derived from molecular topology. *J. Chem. Inf. Comput. Sci.*, 41:147–158, 2001.

Paul C. D. Hawkins, A. Geoffrey Skillman, Gregory L. Warren, Benjamin A. Ellingson, and Matthew T. Stahl. Conformer generation with OMEGA: algorithm and validation using high quality structures from the protein databank and cambridge structural database. *Journal of Chemical Information and Modeling*, 50(4):572–584, 2010.

Kexin Huang, Tianfan Fu, Wenhao Gao, Yue Zhao, Yusuf Roohani, Jure Leskovec, Connor W. Coley, Cao Xiao, Jimeng Sun, and Marinka Zitnik. Therapeutics data commons: Machine learning datasets and tasks for drug discovery and development. *Proceedings of Neural Information Processing Systems, NeurIPS Datasets and Benchmarks*, 2021.

F. Jamali, R. Mehvar, and F.M. Pasutto. Enantioselective aspects of drug action and disposition: therapeutic pitfalls. *Journal of Pharmaceutical Sciences*, 78(9):695–715, 1989.

John Jumper, Richard Evans, Alexander Pritzel, Tim Green, Michael Figurnov, Olaf Ronneberger, Kathryn Tunyasuvunakool, Russ Bates, Augustin Žídek, Anna Potapenko, Alex Bridgland, Clemens Meyer, Simon A. A. Kohl, Andrew J. Ballard, Andrew Cowie, Bernardino Romera-Paredes, Stanislav Nikolov, Rishub Jain, Jonas Adler, Trevor Back, Stig Petersen, David Reiman, Ellen Clancy, Michal Zielinski, Martin Steinegger, Michalina Pacholska, Tamas Berghammer, Sebastian Bodenstein, David Silver, Oriol Vinyals, Andrew W. Senior, Koray Kavukcuoglu, Pushmeet Kohli, and Demis Hassabis. Highly accurate protein structure prediction with alphafold. *Nature*, 596:583–589, 2021.

Steven Kearnes, Kevin McCloskey, Marc Berndl, Vijay Pande, and Patrick Riley. Molecular graph convolutions: Moving beyond fingerprints. *arXiv preprint arXiv:1603.00856*, 2016.

Diederik P. Kingma and Jimmy Ba. Adam: A method for stochastic optimization. *arXiv preprint arXiv:1412.6980*, 2014.

Johannes Klicpera, Shankari Giri, Johannes T. Margraf, and Stephan Günnemann. Fast and uncertainty-aware directional message passing for non-equilibrium molecules. *arXiv preprint arXiv:2011.14115*, 2020a.

Johannes Klicpera, Janek Groß, and Stephan Günnemann. Directional message passing for molecular graphs. *arXiv preprint arXiv:2003.03123*, 2020b.

Johannes Klicpera, Florian Becker, and Stephan Günnemann. GemNet: Universal directional graph neural networks for molecules. *arXiv preprint arXiv:2106.08903*, 2021.

Assia Kovatcheva, Alexander Golbraikh, S. Oloff, J. Feng, W. Zheng, and Alexander Tropsha. QSAR modeling of datasets with enantioselective compounds using chirality sensitive molecular descriptors. *SAR and QSAR in Environmental Research*, 16(1-2):93–102, 2007.

Greg Landrum. RDKit: Open-source cheminformatics. 2010. URL https://www.rdkit.org/.

Kuangbiao Liao, Yun-Fang Yang, Yingzi Li, Jacob N. Sanders, K.N. Houk, Djamaladdin G. Musaev, and Huw M.L. Davies. Design of catalysts for site-selective and enantioselective functionalization of non-activated primary C–H bonds. *Nature Chemistry*, 10:1048–1055, 2018.

Richard Liaw, Eric Liang, Robert Nishihara, Philipp Moritz, Joseph E. Gonzalez, and Ion Stoica. Tune: A research platform for distributed model selection and training. *arXiv preprint arXiv:1807.05118*, 2018.

Zhiqiu Lin, Jin Sun, Abe Davis, and Noah Snavely. Visual chirality. *arXiv preprint arXiv:2006.09512*, 2020.

Yi Liu, Limei Wang, Meng Liu, Xuan Zhang, Bora Oztekin, and Ji Shuiwang. Spherical message passing for 3D graph networks. *arXiv preprint arXiv:2102.05013*, 2021.

Gómez-Hortigüela Luis and Bernardo-Maestro Beatriz. *Chiral Organic Structure-Directing Agents. In: Gómez-Hortigüela, Luis (eds) Insights into the Chemistry of Organic Structure-Directing Agents in the Synthesis of Zeolitic Materials. Structure and Bonding*, volume 175. Springer International Publishing, 2018.

Rafael Mamede, Bruno Simões de Almeida, Mengyao Chen, Qingyou Zhang, and Joao Aires-de Sousa. Machine learning classification of one-chiral-center organic molecules according to optical rotation. *Journal of Chemical Information and Modeling*, 61(1):67–75, 2021.

Elman Mansimov, Omar Mahmood, Seokho Kang, and Kyunghyun Cho. Molecular geometry prediction using a deep generative graph neural network. *Scientific Reports*, 9, 2019.

Lien Ai Nguyen, Hua He, and Chuong Pham-Huy. Chiral drugs: An overview. *International Journal of Biomedical Science*, 2(2):85–100, 2006.

Lagnajit Pattanaik, Octavian-Eugen Ganea, Ian Coley, Klavs F. Jensen, William H. Green, and Connor W. Coley. Message passing networks for molecules with tetrahedral chirality. *arXiv preprint arXiv:2012.00094*, 2020a.

Lagnajit Pattanaik, John B Ingraham, Colin A Grambow, and William H Green. Generating transition states of isomerization reactions with deep learning. *Physical Chemistry Chemical Physics*, 22(41):23618–23626, 2020b.

Andreas Pfaltz and William J. III Drury. Design of chiral ligands for asymmetric catalysis: From C2-symmetric P,P- and N,N-ligands to sterically and electronically nonsymmetrical P,N-ligands. *PNAS*, 101(16):5723–5726, 2004.

Reaxys. Reaxys and the Reaxys trademark are owned and protected by Reed Elsevier Properties SA and used under license. Accessed Aug. 6-9, 2021. URL https://www.reaxys.com/.

Victor Garcia Satorras, Emiel Hoogeboom, and Max Welling. E(n) equivariant graph neural networks. *Proceedings of the 38th International Conference on Machine Learning, PMLR*, 139: 9323–9332, 2021.

Nadine Schneider, Richard A. Lewis, Nikolas Fechner, and Peter Ertl. Chiral cliffs: Investigating the influence of chirality on binding affinity. *ChemMedChem*, 13(13):1315–1324, 2018.

Kristof T. Schütt, Pieter-Jan Kindermans, Huziel E. Sauceda, Stefan Chmiela, Alexandre Tkatchenko, and KLaus-Robert Müller. SchNet: A continuous-filter convolutional neural network for modeling quantum interactions. *arXiv preprint arXiv:1706:08566*, 2017.

Gregor Simm and Jose Miguel Hernandez-Lobato. A generative model for molecular distance geometry. *Proceedings of the 37th International Conference on Machine Learning, PMLR*, 119: 8949–8958, 2020.

Martin Simonovsky and Nikos Komodakis. Dynamic edge-conditioned filters in convolutional neural networks on graphs. *arXiv preprint arXiv:1704.02901*, 2017.

Nathaniel Thomas, Tess Smidt, Steven M. Kearnes, Lusann Yang, Li Li, Kai Kohlhoff, and Patrick Riley. Tensor field networks: Rotation- and translation-equivariant neural networks for 3D point clouds. *arXiv preprint arXiv:1802.08219*, 2018.

Oleg Trott and Arthur J. Olson. AutoDock Vina: improving the speed and accuracy of docking with a new scoring function, efficient optimization and multithreading. *Journal of Computational Chemistry*, 31(2):455–461, 2010.

José R. Valdés-Martiní, Yovani Marrero-Ponce, César R. García-Jacas, Karina Martinez-Mayorga, Stephen J. Barigye, Yasser Silveira Vaz d'Almeida, Facundo Pérez-Giménez, and Carlos A. Morell. QuBiLS-MAS, open source multi-platform software for atom-and bond-based topological (2D) and chiral (2.5 D) algebraic molecular descriptors computations. *Journal of Cheminformatics*, 9(1):1–26, 2017.

Petar Veličković, Guillem Cucurull, Arantxa Casanova, Adriana Romero, Pietro Liò, and Yoshua Bengio. Graph attention networks. *arXiv preprint arXiv:1710.10903*, 2018.

Jan Weinreich, Nicholas J. Browning, and O. Anatole von Lilienfeld. Machine learning of free energies in chemical compound space using ensemble representations: Reaching experimental uncertainty for solvation. *The Journal of Chemical Physics*, 154(13), 2021.

Robin Winter, Frank Noé, and Djork-Arné Clevert. Auto-encoding molecular conformations. *arXiv preprint arXiv:2101.01618*, 2021.

Minkai Xu, Shitong Luo, Yoshua Bengio, Jian Peng, and Jian Tang. Learning neural generative dynamics for molecular conformation generation. *International Conference on Learning Representations (ICLR)*, 2021.

Kevin Yang, Kyle Swanson, Wengong Jin, Connor W. Coley, Philipp Eiden, Hua Gao, Angel Guzman-Perez, Timothy Hopper, Brian Kelley, Miriam Mathea, Andrew Palmer, Volker Settels, Tommi Jaakola, Klavs F. Jensen, and Regina Barzilay. Analyzing learned molecular representations for property prediction. *Journal of Chemical Information and Modeling*, 59(8):3370–3388, 2019.

Raymond A. Yeh, Yuan-Ting Hu, and Alexander G. Schwing. Chirality nets for human pose regression. *arXiv preprint arXiv:1911.00029*, 2019.

Dmitry V. Zankov, Maxim D. Shevelev, Aleksandra V. Nikoenko, Pavel G. Polishchuk, Asima I. Rakhimbekova, and Timur I. Madzhidov. Multi-instance learning for structure-activity modeling for molecular properties. *International Conference on Analysis of Images, Social Networks and Texts*, pp. 62–71, 2019.

Dmitry V. Zankov, Mariia Matveieva, Aleksandra Nikoenko, Ramil Nugmanov, Igor I. Baskin, Alexandre Varnek, Pavel Polishchuk, and Timur Madzhidov. QSAR modeling based on conformation ensembles using a multi-instance learning approach. *Journal of Chemical Information and Modeling*, 2021.

A APPENDIX

CONTENTS

A.1 WHY DOES PLOTTING $\alpha_{\text{SIN}}^{(xy)}$ VS. $\alpha_{\text{COS}}^{(xy)}$ YIELD A PERFECT CIRCLE?

It is not immediately obvious that plotting $\alpha_{\text{sin}}^{(xy)}$ versus $\alpha_{\text{cos}}^{(xy)}$ forms a perfect circle with a constant radius, as opposed to an ellipse or other shape with non-constant radii. Yet, this result follows from simple trigonometry.

From Equation 11, we have:

$$\alpha_{\text{cos}}^{(xy)} = \sum_{i \in N(x) \setminus \{y\}} \sum_{j \in N(y) \setminus \{x\}} c_{ij}^{(xy)} \cos(\psi_{ixyj} + \varphi_{ixyj})$$

$$\alpha_{\text{sin}}^{(xy)} = \sum_{i \in N(x) \setminus \{y\}} \sum_{j \in N(y) \setminus \{x\}} c_{ij}^{(xy)} \sin(\psi_{ixyj} + \varphi_{ixyj})$$

for a internal molecular bond between nodes (x, y) that forms a set of coupled torsions $\{\psi_{ixyj}\}_{(i,j)}$ where $i \in N(x) \setminus \{y\}$ and $j \in N(y) \setminus \{x\}$. For clarity, we drop the (xy) notation and index each torsion in this set of n coupled torsions by a single index k such that $\{\psi_{ixyj}\}_{(i,j)} = \{\psi_k\}_{k=1}^n$.

We want to show that plotting $\sum_{k=1}^n c_k \sin(R + \psi_k + \varphi_k)$ versus $\sum_{k=1}^n c_k \cos(R + \psi_k + \varphi_k)$, where $R \in [0, 2\pi)$ is a rotation of the bond (x, y), yields a circle with a constant radius invariant to the rotation R. As a simple case, consider $n = 2$. We then have:

$$\alpha_{\text{cos}} = c_1 \cos(R + \psi_1 + \varphi_1) + c_2 \cos(R + \psi_2 + \varphi_2) = c_1 \cos(R + \theta_1) + c_2 \cos(R + \theta_2)$$

$$\alpha_{\text{sin}} = c_1 \sin(R + \psi_1 + \varphi_1) + c_2 \sin(R + \psi_2 + \varphi_2) = c_1 \sin(R + \theta_1) + c_2 \sin(R + \theta_2)$$

α_{cos} can be expanded and simplified as:

$$c_1 \cos(R + \theta_1) + c_2 \cos(R + \theta_2) =$$

$$c_1 \Big(\cos(R) \cos(\theta_1) - \sin(R) \sin(\theta_1) \Big) + c_2 \Big(\cos(R) \cos(\theta_2) - \sin(R) \sin(\theta_2) \Big) =$$

$$a \cos(R) - b \sin(R) = d \cos(R + e)$$

where

$$a = d \cos e = c_1 \cos(\theta_1) + c_2 \cos(\theta_2)$$
$$b = d \sin e = c_1 \sin(\theta_1) + c_2 \sin(\theta_2)$$

Similarly, α_{sin} can be expanded and simplified as:

$$c_1 \sin(R + \theta_1) + c_2 \sin(R + \theta_2) =$$

$$c_1 \Big(\sin(R) \cos(\theta_1) + \cos(R) \sin(\theta_1) \Big) + c_2 \Big(\sin(R) \cos(\theta_2) + \cos(R) \sin(\theta_2) \Big) =$$

$$a' \sin(R) + b' \cos(R) = d' \sin(R + e')$$

where

$$a' = d' \cos e' = c_1 \cos(\theta_1) + c_2 \cos(\theta_2)$$
$$b' = d' \sin e' = c_1 \sin(\theta_1) + c_2 \sin(\theta_2)$$

Since $d = d'$ and $e = e'$, we have that $\alpha_{\text{cos}} = d \cos(R + e)$ and $\alpha_{\text{sin}} = d \sin(R + e)$. It follows that in the general case ($n \geq 2$):

$$\alpha_{\text{cos}} = \sum_{k=1}^n c_k \cos(\omega t + \psi_k + \varphi_k) = r \cos(R + s)$$

$$\alpha_{\text{sin}} = \sum_{k=1}^n c_k \sin(\omega t + \psi_k + \varphi_k) = r \sin(R + s)$$

for some coefficients r and s, where $R \in [0, 2\pi)$ represents some rotation about the internal bond. It is immediately obvious that plotting α_{sin} versus α_{cos} for all $R \in [0, 2\pi)$ yields a perfect circle with radius r.

A.2 WHY DO WE NEED PHASE SHIFTS?

At first glance, it is unclear as to why Equations 8-9 are insufficient to learn chirality, e.g. why we need to add phase shifts to distinguish enantiomers. To understand why this is the case, consider an arbitrary stereoisomer containing an internal molecular bond between nodes x and y (with x or y being chiral) that forms a set of n coupled torsions $\{\psi_{ixyj}\}_{(i,j)} = \{\psi_{xy}^{(k)}\}_{k=1}^{n}$ indexed by k. Direct computation of the norm $||\alpha_{\cos}^{(xy)}, \alpha_{\sin}^{(xy)}|| = ||\alpha_{\cos}, \alpha_{\sin}||$ yields:

$$||\alpha_{\cos}, \alpha_{\sin}|| = \sqrt{\alpha_{\cos}^2 + \alpha_{\sin}^2}$$

where we have dropped the (xy) notation for clarity. Expanding and squaring Equation 8 gives:

$$\alpha_{\cos}^2 = \sum_{k=1}^{n} c_k^2 \cos^2 \psi_k + \sum_{k=1}^{n} \sum_{l=k+1}^{n} 2 c_k c_l \cos \psi_k \cos \psi_l$$

$$\alpha_{\sin}^2 = \sum_{k=1}^{n} c_k^2 \sin^2 \psi_k + \sum_{k=1}^{n} \sum_{l=k+1}^{n} 2 c_k c_l \sin \psi_k \sin \psi_l$$

Now consider reflecting this stereoisomer across a plane to generate its enantiomer with inverted chiral centers. Reflecting a conformer negates all its torsions, and thus the reflected enantiomer's internal bond between (reflected) nodes x' and y' will form a set of n negated torsions $\{\psi'_{ixyj}\}_{(i,j)} = \{\psi_{xy}'^{(k)}\}_{k=1}^{n}$ where $\psi_{xy}'^{(k)} = -\psi_{xy}^{(k)}$ for each k. Because enantiomers have the same 2D graph connectivity, the learned set of coefficients $\{c_k\}$ (which depend only on the permutation invariant node features, see Equation 5) will be identical between enantiomers. It immediately follows from the identities $\sin(-x) = -\sin(x)$ and $\cos(-x) = \cos(x)$ that $\alpha_{\cos}'^2 = \alpha_{\cos}^2$ and $\alpha_{\sin}'^2 = \alpha_{\sin}^2$. Because $||\alpha_{\cos}, \alpha_{\sin}||$ is invariant to any rotation of the bond (x, y), no matter how we rotate (x, y) or (x', y'), $||\alpha_{\cos}, \alpha_{\sin}|| = ||\alpha'_{\cos}, \alpha'_{\sin}||$.

Table 4: Effects of ablating components of ChIRo on test-set accuracies for the $l \, / \, d$ classification and enantiomer docking score ranking tasks, when chiral message passing is included prior to readout. Mean and standard deviations are reported across 5 folds ($l \, / \, d$) or 3 repeated trials (enantiomer ranking). The first row indicates the original ChIRo without CMP.

Model Components				Accuracy (%) ↑	
CMP	Tags	$(d_{ij}, \phi_{ijk}, \psi_{ixyj})$	$(\mathbf{z}_d, \mathbf{z}_\phi, \mathbf{z}_\alpha)$	$l \, / \, d$	Enantiomer Ranking
X	X	✓	✓	**79.3 ± 0.4**	**72.0 ± 0.5**
✓	X	✓	✓	78.5 ± 0.5	71.5 ± 0.5
✓	✓	✓	✓	77.0 ± 0.5	71.7 ± 0.6
✓	✓	X	✓	75.1 ± 0.3	69.8 ± 0.6
✓	✓	X	X	75.0 ± 0.9	68.9 ± 0.4
✓	X	X	✓	50.0 ± 0.0	49.9 ± 0.3

A.3   CHIRAL MESSAGE PASSING

Tetrahedral chirality is fundamentally a node-level property. Yet, we have treated chirality through the lens of torsions and internal bonds involving chiral centers. To propagate the learned representations of chirality to node states, we may perform an (optional) additional phase of message passing, treating each $\mathbf{z}_{\alpha_{xy}}$ as a vector of edge-attributes. This might allow the model to propagate chiral information across the graph, i.e., help learn the global effects of local chirality. This phase may be included prior to readout, and uses a single EConv layer followed by a sequence of T_{CMP} GAT layers:

$$\mathbf{h}_i^{\mathrm{CMP}} = \mathrm{GAT}_{\mathrm{CMP}}^{T_{\mathrm{CMP}}} \circ ... \circ \mathrm{GAT}_{\mathrm{CMP}}^1 \Big(\boldsymbol{\Theta}_{\mathrm{CMP}} \, \mathbf{h}_i^T + \sum_{j \in N(i)} \mathbf{h}_j^T \cdot f_{\mathrm{CMP}}(\mathbf{z}_{\alpha_{ij}}) \Big) \tag{15}$$

During readout, these updated node states $\mathbf{h}_i^{\mathrm{CMP}}$ are summed rather than the (non-chiral) node states.

Table 4 reports the effects of including chiral message passing on ChIRo's performance on the $l \, / \, d$ classification task and the ranking enantiomers by docking scores task, along with the effects of ablating other components of ChIRo. Although CMP does not improve performance (and marginally hurts) the unablated ChIRo, using CMP in place of $(\mathbf{z}_d, \mathbf{z}_\phi, \mathbf{z}_\alpha)$ during readout provides another option of augmenting 2D GNNs that solely use chiral tags as the only indication of chirality.

A.4   MODEL ARCHITECTURES

A.4.1   CHIRO

Figure 4 visualizes the full architecture of ChIRo. Table 5 specifies the hyperparameters chosen for each task. See appendix A.6 for details on hyperparameter optimizations.
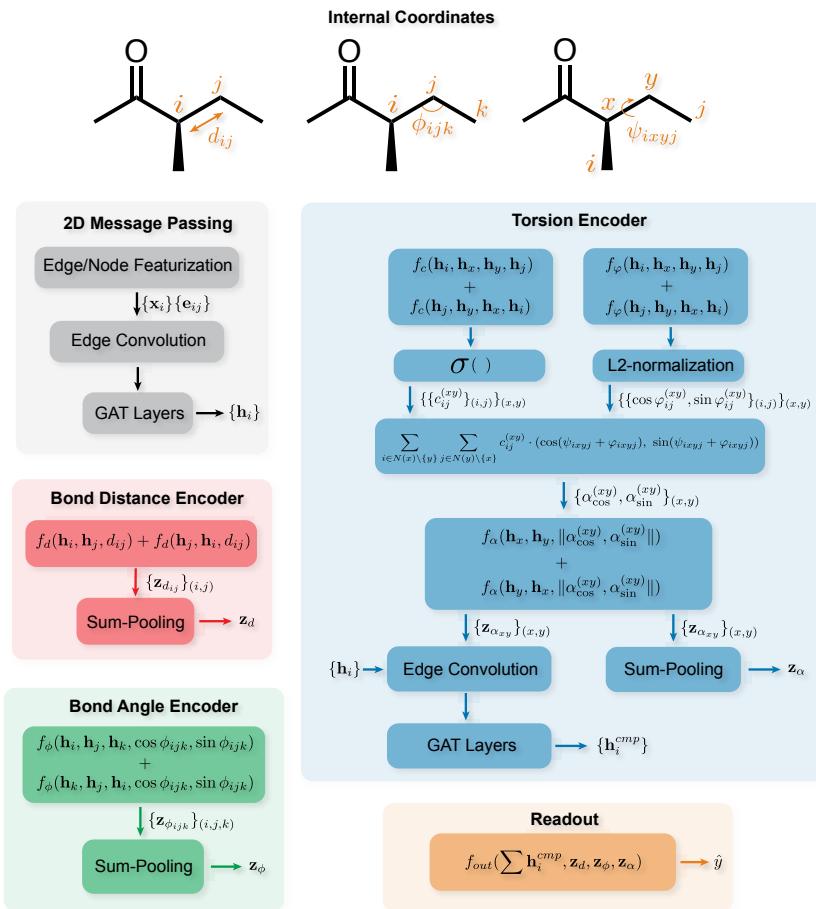
Figure 4: Architecture of ChIRo

Table 5: Hyperparameters optimized for ChIRo on each task. Parameters for chiral message passing are shown, although chiral message passing is omitted in the default version of ChIRo.

Hyperparameters	Task			
	Contrastive	R / S	l / d	Ranking
Node Features Dimension		52		
Edge Features Dimension		14		
All MLP Hidden Activations		LeakyReLU		
All MLP Output Activations		Identity		
EConv MLP Hidden Layer Size	32	64	64	32
EConv MLP # Hidden Layers	2	1	1	32
$\mathbf{h}_0, \mathbf{h}_T, \mathbf{h}_t^{\mathrm{CMP}}$ Dimension	64	32	32	64
$\mathbf{h}_t, t = 1, ..., T - 1$ Dimension	64	64	32	64
# GAT Layers	2	3	2	2
# GAT Heads	4	4	2	4
f_d Hidden Layer Size	–	128	32	64
f_d # Hidden Layers	–	2	2	2
f_ϕ Hidden Layer Size	–	128	32	64
f_ϕ # Hidden Layers	–	2	2	2
f_α Hidden Layer Size	64	128	32	64
f_α # Hidden Layers	2	2	2	2
f_c Hidden Layer Size	64	128	32	64
f_c # Hidden Layers	2	2	2	2
f_φ Hidden Layer Size	64	256	256	256
f_φ # Hidden Layers	2	2	3	2
f_{out} Hidden Layer Size	–	64	64	128
f_{out} # Hidden Layers	–	2	2	2
CMP EConv Hidden Layer Size	–	32	256	256
CMP EConv # Hidden Layers	–	1	3	2
# CMP GAT Layers	–	3	3	3
# CMP GAT Heads	–	2	2	2
γ_{aux}	8.25e-4	6.86e-3	1.86e-3	8.25e-4
Learning Rate	6.06e-4	5.69e-4	1.28e-4	6.06e-4
Batch Size	32	16	16	32
# Epochs	50	100	100	150

Table 6: Hyperparameters selected for SphereNet on each task. See appendix A.6 for hyperparameter optimizations.

Hyperparameters	Task			
	Contrastive	R / S	l / d	Ranking
Readout MLP Hidden Activations		LeakyReLU		
Readout MLP Output Activation		Identity		
Readout MLP Hidden Size	–	256	64	64
Readout MLP # of Hidden Layers	–	4	2	2
hidden_channels	128	256	64	256
out_channels	2	64	64	32
cutoff	5.0	5.0	5.0	5.0
num_layers	4	4	4	5
int_emb_size	64	32	128	64
basis_emb_size_dist	8	8	8	8
basis_emb_size_angle	8	8	8	8
basis_emb_size_torsion	8	8	8	8
out_emb_channels	256	128	64	32
num_spherical	7	7	7	7
num_radial	6	6	6	6
envelope_exponent	5	5	5	5
num_before_skip	1	1	1	1
num_after_skip	2	2	2	2
num_output_layers	3	3	3	3
Learning Rate	1e-4	1.54e-4	4.79e-4	1.40e-4
Batch Size	32	64	16	32

A.4.2 3D BASELINES

To adapt SchNet, DimeNet++, and SphereNet for our tasks, we increase the dimensionality of their respective aggregated node embeddings ("out_channels") and use this aggregation as a latent vector either for direct use in Equation 14 (for self-supervised contrastive learning), or for input to a feed-forward readout MLP for downstream regression/classification. For all three 3D GNNs, we use their default node featurizations, using the atomic number as the only node feature.

Table 6 lists the hyperparameters used for SphereNet on all four tasks. Tables 7 and 8 list the hyperparameters used for SchNet and DimeNet++ on the contrastive learning and R / S classification tasks.

Table 7: Hyperparameters selected for SchNet on each task. Apart from the number of out channels and the inclusion of a readout MLP, the default SchNet architecture was used. Note that we used the same readout MLP architecture as in the optimized SphereNet.

Hyperparameters	Task	
	Contrastive	R / S
Readout MLP Hidden Activations	–	LeakyReLU
Readout MLP Output Activation	–	Identity
Readout MLP Hidden Size	–	64
Readout MLP # of Hidden Layers	–	2
hidden_channels	128	128
out_channels	2	32
num_filters	128	128
num_interactions	6	6
num_gaussians	50	50
cutoff	10.0	10.0
max_num_neighbors	32	32
Learning Rate	1e-4	1e-4
Batch Size	32	32

Table 8: Hyperparameters selected for DimeNet++ on each task. Apart from the number of out channels and the inclusion of a readout MLP, the default DimeNet++ architecture was used. Note that we used the same readout MLP architecture as in the optimized SphereNet.

Hyperparameters	Task	
	Contrastive	R / S
Readout MLP Hidden Activations	–	LeakyReLU
Readout MLP Output Activation	–	Identity
Readout MLP Hidden Size	–	64
Readout MLP # of Hidden Layers	–	2
hidden_channels	128	128
out_channels	2	32
num_blocks	4	4
cutoff	5.0	5.0
int_emb_size	64	64
basis_emb_size	8	8
out_emb_channels	256	256
num_spherical	7	7
num_radial	6	6
envelope_exponent	5	5
num_before_skip	1	1
num_after_skip	2	2
num_output_layers	3	3
Learning Rate	1e-4	1e-4
Batch Size	32	32

Table 9: Hyperparameters selected for DMPNN on each task. Following Pattanaik et al., we only optimize hyperparameters for the baseline sum aggregator and extend these hyperparameters to the TetraDMPNN models.

Hyperparameters	Task	
	Contrastive	R / S
hidden_size	300	300
depth	3	3
dropout	0.2	0.2
Max Learning Rate	1e-4	1e-4
Batch Size	50	50

A.4.3   2D BASELINES

To optimize hyperparameters for all 2D baselines, we directy use the code provided by Pattanaik et al.. We do not make any modifications to the architectures, since we train on similar tasks as the original work.

A.5 TRAINING DETAILS

This section describes the full training protocols for each task considered in this paper.

A.5.1 DIMENET++ INITIALIZATIONS

The default parameter initializations for the output blocks of DimeNet++ make DimeNet++ unable to break symmetry between different output channels when the number of output channels is set > 1. Thus, we remove the default initializations for the output blocks when training DimeNet++ on the contrastive learning task (out_channels = 2) and the R/S classification task (out_channels = 32).

A.5.2 SPHERENET DATA PROCESSING ERRORS

When training SphereNet, occasionally the publicly-available implementation of SphereNet failed to process select conformers. Because this occurred for only a tiny fraction of the conformers in the overall datasets, we removed 2D graphs whose stereoisomers contained problematic conformers from the R/S and l / d datasets *for SphereNet only*. We emphasize that this filtering step did not meaningfully change the size of the datasets: only 40 2D graphs (out of 39,256) were removed for the R/S task, and only 6 2D graphs (out of 15,038) were removed for the l / d task. No molecules had to be removed for the ranking enantiomers by docking scores task. For the contrastive learning task, we simply skipped the rare batch during training/inference that contained problematic conformers. Only 452 2D graphs out of 257,743 caused processing errors in the contrastive learning dataset.

A.5.3 AUXILIARY TORSION LOSS WHEN TRAINING CHIRO

In Equation 10, we predict an angular phase shift φ by using f_φ to predict $\cos\varphi$ and $\sin\varphi$ separately with a *linear* output activation, and then use ℓ_2 normalization on the vector $[\cos\varphi, \sin\varphi]$ to ensure that these $\sin$ and $\cos$ (and thus the angle φ) have correct circular properties, namely that $\varphi \in [0, 2\pi)$. We have chosen to predict angles using $\sin$ and $\cos$ rather than directly predicting a scalar $\varphi \in [0, 2\pi)$ (e.g., through a scaled sigmoid activation) in order to avoid biasing the predicted phase shifts toward 0. However, the ℓ_2 normalization can also cause the predicted phase shift to be biased toward 0, $\pi/2$, π, and $3\pi/2$ if one of the *unnormalized* $\cos\varphi$ or $\sin\varphi$ blows up. To prevent this, we follow Jumper et al. (2021) in adding an auxiliary loss during training to encourage the unnormalized $[\cos\varphi, \sin\varphi]$ to fall close to the unit circle:

$$L_{\text{aux}} = \gamma_{\text{aux}}(1 - ||\cos\varphi, \sin\varphi||) \tag{16}$$

where γ_{aux} is a small scalar that is tuned during hyperparameter optimization.

A.5.4 CONTRASTIVE LEARNING

For contrastive learning, we train with a triplet margin loss with a normalized Euclidean distance metric and a margin of 1 (Equation 14). In each training epoch, we randomly partition the training data into N/b minibatches, where N is the number of distinct *stereoisomers* (not conformers) in the training set and b is the batch size. Before triplet sampling, each minibatch therefore contains b stereoisomers. For each stereoisomer $i = (1, 2, ..., b)$ in the minibatch, we then generate a triplet (a, p, n), where a (anchor) and p (positive) are two randomly selected (without replacement) conformers of stereoisomer i, and n (negative) is a randomly selected conformer of stereoisomer $j \neq i$, where i and j share the same 2D graph connectivity. If stereoisomer i has multiple different stereoisomers $j, k, ...$ (all sharing the same 2D graph) present in the training set, one of these stereoisomers is randomly chosen. Each anchor, positive, and negative in each triplet are processed independently by the network to generate b triplets of latent vectors $(\mathbf{z}_a, \mathbf{z}_p, \mathbf{z}_n)$, which are then fed into the triplet margin loss function. Loss contributions from each triplet are averaged to form a loss for the entire batch. In the case of ChIRo, we add the mean auxiliary torsion loss across all *conformers* in the batch to the batch triplet loss.

We use the Adam optimizer (Kingma & Ba, 2014) with a flat learning rate throughout training, but employ gradient clipping with a maximum gradient L2-norm of 10. We train each model for a maximum of 50 epochs, and use the batch-averaged triplet loss (without the auxiliary torsion loss contributions) on the validation set to select the model with the best estimated generalization performance across the 50 epochs. We do not employ dropout or other forms of explicit regularization.

A.5.5 R / S CLASSIFICATION

For R / S classification, we train each 3D model with a binary cross-entropy loss. In each training epoch, we randomly partition the training data into N/b minibatches, where N is the number of *enantiomers* in the training set and b is the batch size. For each enantiomer in the batch, we randomly sample a conformer for that enantiomer *and* a conformer for its opposite enantiomer with the same 2D graph. This ensures that minibatches contain both enantiomers of the enantiomeric pair such that the stochastic gradient steps consider contributions from both enantiomers. We average the loss contributions for all conformers in the batch. In the case of ChIRo, the mean auxiliary torsion loss across all conformers in the batch is added to the batch cross-entropy loss.

We use the Adam optimizer with a flat learning rate throughout training, but employ gradient clipping with a maximum gradient L2-norm of 10. We train each model for a maximum of 100 epochs, and use the batch-averaged *classification accuracy* on the validation set to select the model with the best estimated generalization performance across the 100 epochs. We do not employ dropout or other forms of explicit regularization.

For testing, we evaluate the classification accuracy on *all* conformers in the test set, and do not use any form of conformer-based averaging or voting.

A.5.6 *l / d* CLASSIFICATION

For *l / d* classification, we train each model with a binary cross-entropy loss. In each training epoch, we randomly partition the training data into N/b minibatches, where N is the number of *enantiomers* in the training set and b is the batch size. For each enantiomer in the batch, we sample either 1) a random conformer *or* 2) a pre-selected conformer for that enantiomer, *and* either 1) a random conformer *or* 2) a pre-selected conformer conformer for its opposite enantiomer with the same 2D graph. This ensures that minibatches contain both enantiomers of the enantiomeric pair such that the stochastic gradient steps consider contributions from both enantiomers. In both cases, we average the loss contributions for all conformers in the batch. In the case of ChIRo, we add the mean auxiliary torsion loss across all conformers in the batch to the batch cross-entropy loss.

We use the Adam optimizer with a flat learning rate throughout training, but employ gradient clipping with a maximum gradient L2-norm of 10. We train each model for a maximum of 100 epochs, and use the batch-averaged *classification accuracy* on the validation set to select the model with the best estimated generalization performance across the 100 epochs. We do not employ dropout or other forms of explicit regularization.

For testing, we evaluate the classification accuracy on *all* conformers in the test set, and do not use any form of conformer-based averaging or voting.

A.5.7 RANKING ENANTIOMERS BY DOCKING SCORES

For ranking enantiomers by their docking scores, we train each model with a mean squared error (MSE) loss, with the target values being the ground-truth docking scores for each enantiomer. Note that although we train the models with an MSE loss, we are more concerned with the ability of each model to correctly rank enantiomers by their docking scores than with the absolute performance of each model as a surrogate model for docking score prediction. Thus, we *evaluate* this task using the ranking accuracy, defined as whether or not the model correctly predicts a lower docking score for the enantiomer with the lower ground-truth score.

In each training epoch, we randomly partition the training data into N/b minibatches, where N is the number of *enantiomers* in the training set and b is the batch size. For each enantiomer in the batch, we sample either 1) a random conformer *or* 2) a pre-selected conformer for that enantiomer, *and* either 1) a random conformer *or* 2) a pre-selected conformer conformer for its opposite enantiomer with the same 2D graph. This ensures that minibatches contain both enantiomers of the enantiomeric pair such that the stochastic gradient steps consider contributions from both enantiomers. In both cases, we average the loss contributions for all conformers in the batch. In the case of ChIRo, we add the mean auxiliary torsion loss across all conformers in the batch to the batch MSE loss.

We use the Adam optimizer with a flat learning rate throughout training, but employ gradient clipping with a maximum gradient L2-norm of 10. We train each model for a maximum of 150 epochs,

and use the batch-averaged *ranking accuracy* on the validation set to select the model with the best estimated generalization performance across the 150 epochs. We do not employ dropout or other forms of regularization.

For testing, we first predict the docking score for *all* conformers in the test set. We then average the predicted docking scores for each conformer of each enantiomer, yielding a mean predicted score for each enantiomer. Finally, we compute the ranking accuracy using these mean predicted scores.

Table 10: Hyperparameter search space for ChIRo

Hyperparameter	Search Space
EConv MLP Hidden Layer Size	[32, 64, 128, 256]
EConv MLP # Hidden Layers	[1,2]
$\mathbf{h}_0, \mathbf{h}_T, \mathbf{h}_t^{CMP}$ Dimension	[8, 16, 32, 64]
$\mathbf{h}_t, t = 1, ..., T - 1$ Dimension	[16, 32, 64]
# GAT Layers	[2,3,4]
# GAT Heads	[1,2,4,8]
$f_d, f_\phi, f_\alpha, f_c$ Hidden Layer Size	[32, 64, 128, 256]
$f_d, f_\phi, f_\alpha, f_c$ # Hidden Layers	[1,2,3,4]
f_φ Hidden Layer Size	[32, 64, 128, 256]
f_φ # Hidden Layers	[1,2,3,4]
f_{out} Hidden Layer Size	[32, 64, 128, 256]
f_{out} # Hidden Layers	[1,2,3,4]
CMP EConv Hidden Layer Size	[32, 64, 128, 256]
CMP EConv # Hidden Layers	[1,2,3,4]
# CMP GAT Layers	[1, 2, 3, 4]
# CMP GAT Heads	[1, 2, 4, 8]
γ_{aux}	log uniform (1e-4, 1e-2)
Learning Rate	log uniform (5e-5, 5e-3)
Batch Size	[16, 32, 64, 128, 256]

A.6 HYPERPARAMETER OPTIMIZATIONS

A.6.1 CHIRO

Hyperparameters were tuned for ChIRo on the R / S, *l / d*, and ranking enantiomers by docking score tasks, using the Raytune (Liaw et al., 2018) Python package with the HyperOpt plug-in. For the R / S classification and ranking enantiomers by docking score tasks, we tuned hyperparameters by training with the training set and evaluating model accuracy on the validation set. For the *l / d* classification task, we used the training and validation splits of the first cross-validation fold to tune hyperparameters, evaluating model accuracy on the validation split. The optimal hyperparameters were then held constant for the remaining four folds.

For each task below, we used the HyperOptSearch search algorithm in Raytune, which employs Tree-structured Parzen Estimators, to search for optimal hyperparameters over the search space specified in Table 10.

R / S Classification. We trained a total of 100 models with different hyperparameter combinations for a maximum of 50 epochs, using the Async Hyperband Scheduler (grace period = 5, reduction factor = 3, brackets = 1) for aggressive early stopping.

***l / d* Classification** We performed two stages of optimization. We first trained 100 models with different hyperparameter combinations for a maximum of 50 epochs, using the Async Hyperband Scheduler (grace period = 5, reduction factor = 3, brackets = 1) for aggressive early stopping. We then re-ran the optimization for 50 parameter combinations over a maximum of 100 epochs, using the best five models from the first optimization as starting (seed) configurations. In this second stage, we again used HyperOptSearch but changed the Async Hyperband Scheduler to use parameters (grace period = 10, reduction factor = 4, brackets = 1).

Ranking enantiomers by docking score. We trained a total of 100 models with different hyperparameter combinations for a maximum of 50 epochs, using the Async Hyperband Scheduler (grace period = 5, reduction factor = 3, brackets = 1) for aggressive early stopping.

Table 11: Hyperparameter search space for SphereNet

Hyperparameter	Search Space
hidden_channels	[64, 128, 256]
out_channels	[16, 32, 64, 128, 256]
cutoff	[5.0, 10.0]
num_layers	[3,4,5]
int_emb_size	[32, 64, 128]
basis_emb_size_dist	8
basis_emb_size_angle	8
basis_emb_size_torsion	8
out_emb_channels	[64, 128, 256]
num_spherical	7
num_radial	6
envelope_exponent	5
num_before_skip	1
num_after_skip	2
num_output_layers	3
Readout MLP Hidden Size	[32, 64, 128, 256]
Readout MLP # of Hidden Layers	[1,2,3,4]
Learning Rate	log uniform (5e-5, 1e-2)
Batch Size	[16, 32, 64, 128, 256]

Table 12: Hyperparameter search space for DMPNN

Hyperparameter	Search Space
hidden_size	[300, 600, 900, 1200]
depth	[2, 3, 4, 5, 6]
dropout	[0, 0.2, 0.4, 0.6, 0.8, 1]
Max Learning Rate	log uniform (1e-5, 1e-3)
Batch Size	[25, 50, 100]

A.6.2 SPHERENET

Hyperparameters were also tuned for SphereNet on the R / S, *l* / *d*, and ranking enantiomers by docking score tasks, using the same optimization methodologies as when tuning ChIRo. The hyperparameter search space is specified in Table 11. In each of these tasks, we trained a total of 50 models with different hyperparameter combinations for a maximum of 50 epochs, using the Hyper-OptSearch algorithm and the Async Hyperband Scheduler (grace period = 5, reduction factor = 3, brackets = 1) for aggressive early stopping.

A.6.3 DMPNN

We tune hyperparameters for the DMPNN on the *l* / *d* classification and ranking enantiomers by docking score tasks using the original code provided by Pattanaik et al., which employs the Optuna hyperoptimization framework (Akiba et al., 2019). We train a total of 100 models using the HyperbandPruner algorithm to prune unpromising trials and the CmaEsSampler to sample new trials. Note that we only optimize hyperparameters for the sum aggregation baseline model, and we extend these hyperparameters to the TetraDMPNN models, following the work of Pattanaik et al.. Because the TetraDMPNN models use a permutation-based aggregation function, the runtime of these models is much slower, which renders a full hyperparameter optimization infeasible.

A.7 DATASETS

A.7.1 CONTRASTIVE LEARNING AND R/S CLASSIFICATION DATASETS

To create the datasets for the contrastive learning and R/S classification tasks, we first randomly selected 50 sdf files from the "10 conformers per compound" directory from the PubChem3D FTP site `ftp://ftp.ncbi.nlm.nih.gov/pubchem/Compound_3D/`, out of 6199 available. After extracting the conformers in each sdf file, we filtered the data to only include conformers of 2D graphs for which *at least* 2 stereoisomers appear in the data, and where each of these stereoisomers has *at least* 2 conformers in the data. We further filtered the data to only include 2D graphs whose conformers contain at least 1 torsion, as recognized by RDKit. This dataset was separated into 80/20 partitions, with conformers corresponding to the same 2D graph being assigned to the same data partition. The larger (80%) subset was used as-is for contrastive learning. The smaller (20%) subset was further filtered to only include pairs of enantiomers with *only* 1 chiral center, excluding 2D graphs that contained other (cis/trans) stereoisomers of these enantiomer pairs in the dataset. Note that this extra step ensures that there are only two stereoisomers (which are enantiomers) per 2D graph. The resultant subset was used as the R/S classification dataset.

Figures 5 and 6 show the distributions of the number of conformers per stereoisomer and the number of stereoisomers per 2D graph in the full contrastive learning dataset. Figure 7 shows the distribution of the number of conformers per enantiomer in the full R/S classification dataset. Table 13 indicates the distribution of R/S labels in the R/S dataset.

The full contrastive learning dataset was split into 70/15/15 sets for training, validation, and testing, respectively, with conformers corresponding to the same 2D graphs being assigned to the same data partition. The training set contains 2,088,008 conformers of 418,922 stereoisomers of 180,426 distinct 2D graphs. The validation set contains 450,726 conformers of 89,786 stereoisomers of 38,658 distinct 2D graphs. The test set contains 448,017 conformers of 89,914 stereoisomers of 38,659 distinct 2D graphs.

The full R/S dataset was similarly separated into 70/15/15 sets, with pairs of enantiomers being assigned to the same data partition. The training set contains 326,865 conformers of 55,084 stereoisomers (27,542 pairs of enantiomers). The validation set contains 70,099 conformers of 11,748 stereoisomers (5874 pairs of enantiomers). The test set contains 69,719 conformers of 11,680 stereoisomers (5840 pairs of enantiomers).
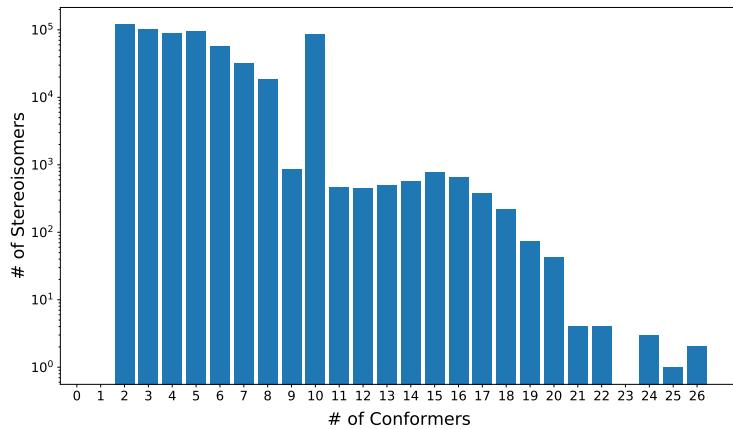

Figure 5: Histogram of the number of conformers per stereoisomer in the contrastive learning dataset.
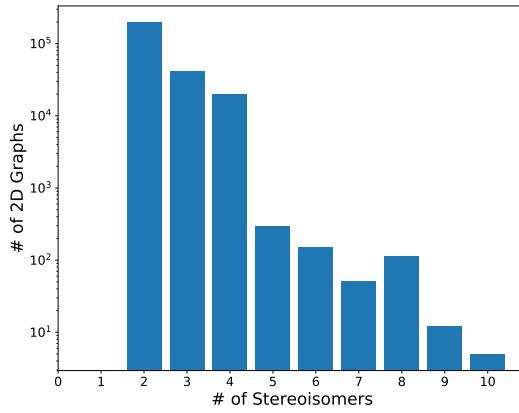
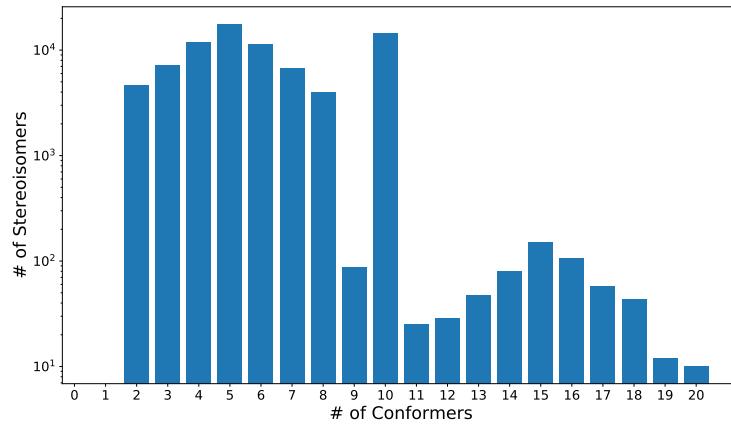Figure 6: Histogram of the number of stereoisomers per 2D graph in the contrastive learning dataset.

Figure 7: Histogram of the number of conformers per enantiomer in the R/S classification dataset.

Table 13: Balance of R/S labels in the R/S classification dataset.

R / S Label	# of Conformers	# of Enantiomers
R	236222	39256
S	230461	39256

A.7.2   *l* / *d* CLASSIFICATION DATASET

Figure 8 enumerates the data filtering steps used to extract and filter the *l* / *d* classification dataset from the experimental Reaxys database. In Reaxys, we queried non-fragmented molecules with molecular weights ≤ 564 which had optical rotatory power reported at 18-30 ^{o}C and a wavelength of 589 nm. We further filtered these molecules to include those with SMILES strings that were validated by RDKit, and those which contained only 1 chiral center. Of these molecules, we removed duplicate entries if they were reported with different signs of optical rotation (which indicates an experimental measurement error). If duplicates had consistent signs of optical rotation, we randomly selected one entry. We then removed entries that did not have full stereochemistry specified in their SMILES strings, since we would later need to generate conformers for each molecule. We also removed molecules whose non-enantiomeric (e.g., cis/trans) stereoisomers also appeared in the dataset. We then checked if pairs of enantiomers were both reported in the dataset, and excluded such pairs if they were reported with the same sign of optical rotation (which indicates an experimental measurement error). For molecules whose opposite enantiomers were not in the dataset, we artificially generated the opposite enantiomer and assigned it the opposite sign of optical rotation. This ensures a balanced dataset. We then selected pairs of enantiomers which were reported with $\geq$ 95% enantiomeric excess in order to reduce the risk of experimental noise causing labeling errors. Lastly, we used RDKit to generate 5 conformers for each enantiomer in the filtered dataset. If RDKit failed to generate a conformer for any pair of enantiomers, both enantiomers in the pair were removed from the dataset.

Table 14 reports the distribution of *l* / *d* labels in the final dataset, which contains 150,380 conformers of 30,076 enantiomers (15,038 pairs of enantiomers). We split this dataset into 5 folds for cross-validation, randomly assigning each pair of enantiomers (with their conformers) to a test set in one of the five folds. For each fold, we randomly split the remaining (i.e., non-testing) pairs of enantiomers into 87.5/12.5 training/validation sets. Note that this ensures each fold has 70/10/20 training/validation/test splits, with pairs of enantiomers being assigned to the same data partition within each fold, and that each pair of enantiomers only appears in one test set across the five folds.
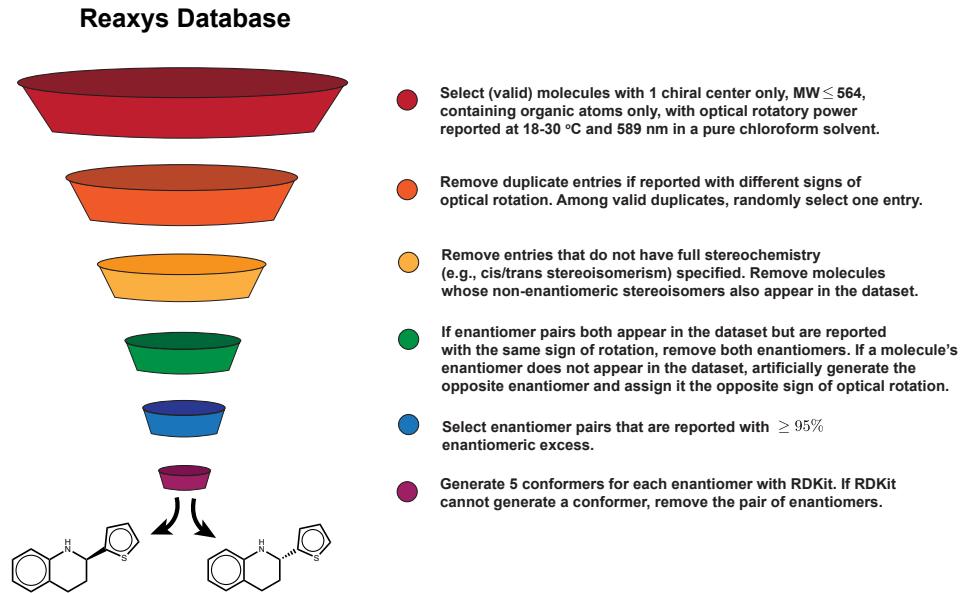
Reaxys Database

Figure 8: Data extraction, filtering, and generation steps for the *l* / *d* classification task.

Table 14: Balance of l / d labels in dataset.

l / d Label	# of Conformers	# of Enantiomers
l	75190	15038
d	75190	15038

Table 15: Frequency of R/S labels amongst enantiomers in the l / d dataset that rotate light in the positive (d) or negative (l) direction. The balance in R/S labels indicates the lack of empirical correlation between these two classification schemes.

	l	d
R	7316	7722
S	7722	7316

A.7.3 RANKING ENANTIOMERS BY DOCKING SCORES

To create the dataset for the ranking enantiomers by their docking scores task, we randomly selected 750 sdf files from the "10 conformers per compound" directory from the PubChem3D FTP site `ftp://ftp.ncbi.nlm.nih.gov/pubchem/Compound_3D/`, out of the 6199 available, but excluding the 50 sdf files used previously for the contrastive learning and R/S classification datasets. After extracting the conformers in each sdf file, we filtered the data to only include conformers of 2D graphs for which *only* 2 stereoisomers (corresponding to pairs of enantiomers with 1 chiral center) appeared in the dataset. As before, we only included enantiomers whose conformers contain at least 1 torsion, as recognized by RDKit. We then filtered enantiomers which have a molecular weight ≤ 225 and ≤ 5 rotatable bonds (as computed by RDKit). This step was designed to intentionally select small enantiomers which had few rotational degrees of freedom such that the docking simulations would be less stochastic. We then docked each pair of enantiomers three times against the protein (PDB ID: 4JBV) in the docking box centered at $[10, 16, 61]$ with (x,y,z) radii of $[10, 14, 12]$. In each docking simulation, we increased the exhaustiveness parameter to 24 to help reduce noise in the resultant docking scores. As a final control for stochasticity in the docking simulations, we also removed pairs of enantiomers for which one or both of the enantiomers had a range of (top) docking scores > 0.1 kcal/mol across the three simulation trials. Finally, in order to select pairs of enantiomers which exhibit meaningful differences in docking scores, we filtered the dataset to only include pairs of enantiomers which had a difference in their best docking scores (across the three trials) of at least 0.3 kcal/mol. These enantiomers and their PubChem3D conformers were used as the final dataset. Figure 9 visualizes the full filtering procedure.

Figure 10 plots the distribution of the number of conformers per enantiomer in the docking dataset. Figure 11 plots the distribution of the difference in docking scores between pairs of enantiomers in the docking dataset. We split the full dataset into 70/15/15 training/validation/test sets, assigning pairs of enantiomers (with their conformers) to the same data partition. The training set contains 234,622 conformers of 48,384 enantiomers (24,192 pairs of enantiomers). The validation set contains 49,878 conformers of 10,368 enantiomers (5184 pairs of enantiomers). The test set contains 50,571 conformers of 10,368 enantiomers (5184 pairs of enantiomers).
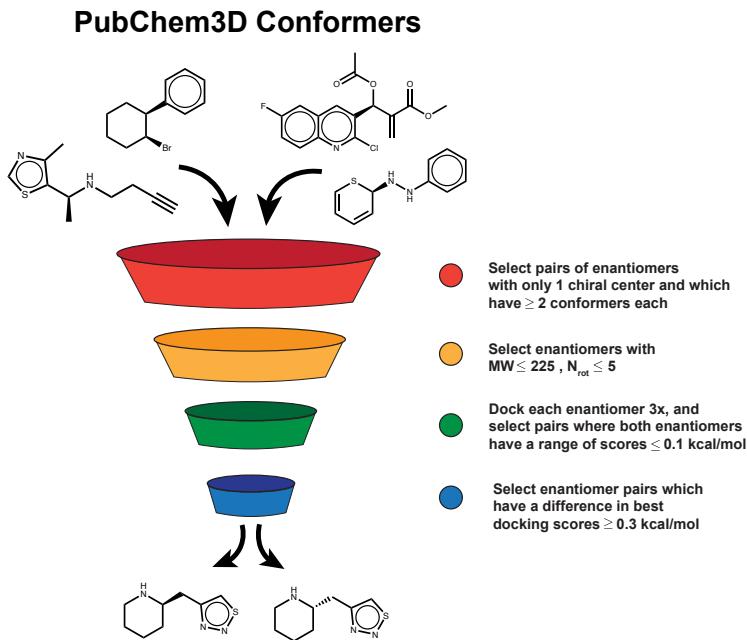

Figure 9: Data generation and filtering steps for the ranking enantiomers by docking scores task.
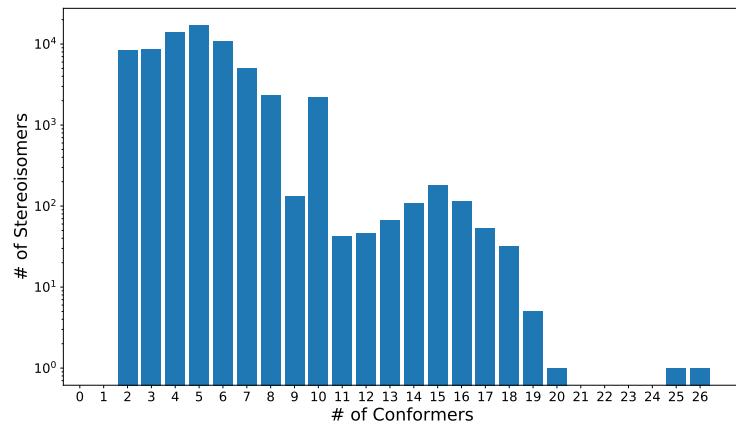
Figure 10: Histogram of the number of conformers per enantiomer in the docking dataset.
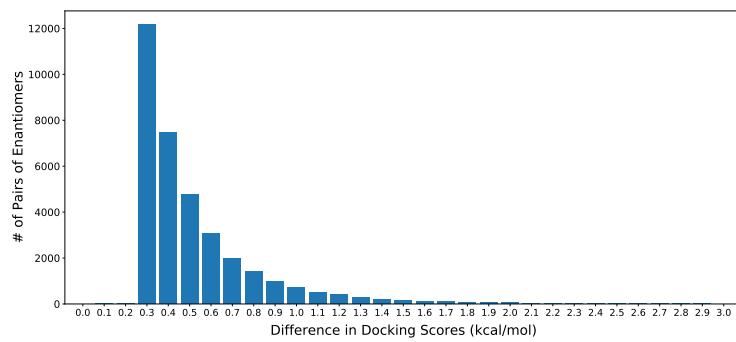

Figure 11: Distribution of the differences in (best) docking scores between pairs of enantiomers in the docking dataset.

A.8 ADDITIONAL ABLATIONS

It is not strictly necessary that ChIRo *learn* the weight coefficients $c_{ij}^{(xy)}$ or phase shifts φ_{ixyj} in order to distinguish enantiomers. ChIRo can still learn chiral representations and preserve invariance to internal bond rotations if $c_{ij}^{(xy)}$ and φ_{ixyj} are generated by networks with random, untrained parameters. To demonstrate this, we perform additional ablations where the feed-forward networks f_c and f_φ are not trained, but rather keep their initial random parameters. Table 16 reports the results of not training these MLPs on the otherwise unchanged ChIRo on the l / d classification task and ranking enantiomers by docking scores task. Overall, learning the parameters in f_c leads to only small (if any) performance gains versus keeping the randomly initialized parameters. On the other hand, learning the parameters in f_φ leads to considerable performance gains versus not learning f_φ. This emphasizes that in our case, relying on random noise to break symmetry between embeddings of enantiomers is insufficient to learn *expressive* chiral representations. Rather, ChIRo best models the effects of chirality by *learning* to break the symmetry through learned phase shifts in a task-specific manner.

Table 16: Effects of not learning the parameters in f_c and f_φ on ChIRo's performance on the l / d classification and the ranking enantiomers by docking score tasks. For the original, unablated ChIRo (first row), mean accuracy and standard deviations on the test sets are reported across 5 folds (l / d) or three repeated trials (enantiomer ranking). To better account for the impact of random network initializations, for the ablated models we report the mean accuracy and standard deviations on the test sets across 3 repeated trials (enantiomer ranking) or the mean, fold-averaged accuracy (e.g., mean of means) and standard error of this mean across three repeated 5-fold CV trials (l / d classification).

Model Components		Accuracy (%) ↑	
Learned f_c	Learned f_φ	l / d	Enantiomer Ranking
✓	✓	79.3 ± 0.4	72.0 ± 0.5
X	✓	79.4 ± 0.3	71.7 ± 0.2
✓	X	53.7 ± 1.2	68.4 ± 0.7
X	X	50.8 ± 0.8	66.8 ± 0.3

A.9 ADDITIONAL EVALUATION OF RANKING ENANTIOMERS BY DOCKING SCORES

Because some enantiomers have larger differences in their ground truth docking scores than other enantiomers, a single ranking accuracy metric may not fully describe the ability of the models to learn the enantioselectivity of the protein pocket. To evaluate model performance more thoroughly, we compute ranking accuracies on various subsets of the test set. Figure 12 plots the ranking accuracies of ChIRo, SphereNet, Tetra-DMPNN (concatenate) with chiral tags, and DMPNN with chiral tags when evaluated on subsets of the test data where the difference in ground truth docking scores are (upper left) greater or equal to a margin, (upper right) less than or equal to a margin, or (bottom) exactly equal to a margin. The plots suggest that while ChIRo is superior in correctly ranking enantiomers which have relatively small differences in their true docking scores, the differences between each model become less distinct when ranking enantiomers with larger differences in their ground-truth docking scores. This may be due to the fact that the docking dataset is imbalanced, skewed heavily toward enantiomers that have smaller differences in their true docking scores (Figure 11).
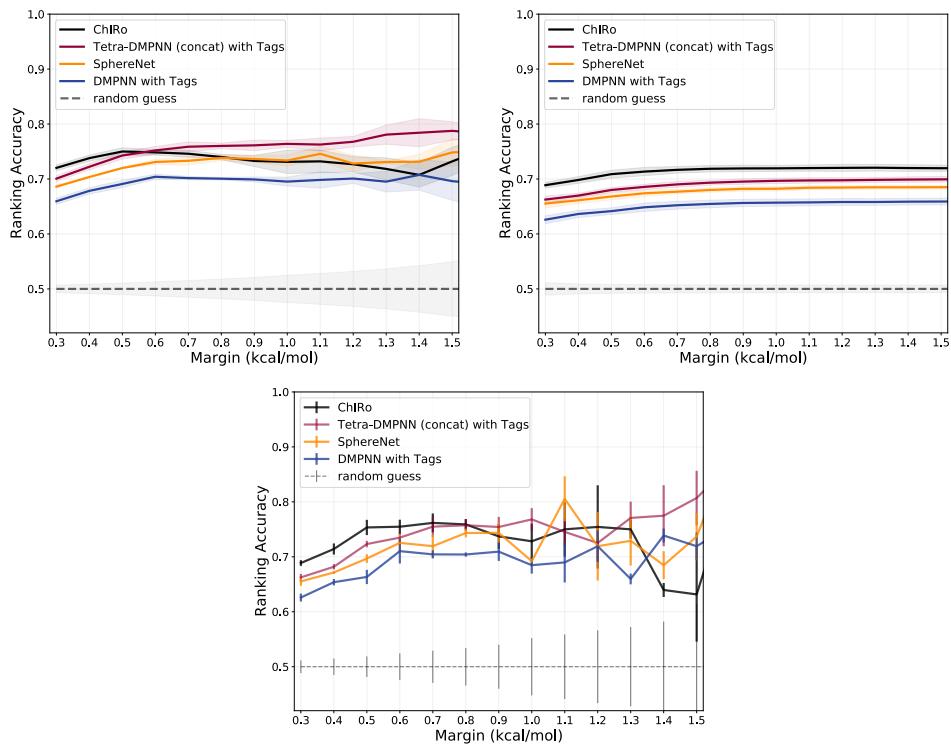
Figure 12: Ranking accuracy of the predicted conformer-averaged docking scores when evaluated on subsections of the test set in which the ground truth difference in best docking scores between enantiomers is (upper left) greater than or equal to the specified margin, (upper right) less than or equal to the specified margin, or (bottom) equal to the specified margin. Error bars for the models represent standard deviations in ranking accuracy across three random training/inference trials. Error bars for the random baseline correspond to the standard deviation of a binomial distribution $B(p = 0.5, N)$, where N is the number of enantiomer pairs in the subset.